Friedrich-Alexander-Universität
Naturwissenschaftliche Fakultät

Bachelor Thesis
in Physics

Investigating microstructures with computed tomography and dark-field imaging

Juan Prior Herrero

Supervisor: Prof. Dr. Stefan Funk

Erlangen Centre for Astroparticle Physics

Submission date: 30-07-25

Contents

1 Introduction

The characterization of internal microstructures is crucial for understanding the performance, reliability, and failure mechanisms of modern materials. As advanced engineering materials such as carbon and titanium composites and fibers are increasingly used in high-performance applications, non-destructive imaging techniques capable of resolving their inner architectures at the micro- and nano-scale have become essential. This thesis explores two powerful modalities: x-ray micro computed tomography (CT) and dark-field imaging to probe the internal structure of two representative materials, a carbon fiber composite and a titanium fiber sample.

Carbon composites and titanium alloys are widely used in aerospace, biomedical, and automotive industries. These materials often have some special mechanical properties, such as high strength to weight ratio and corrosion resistance, due to intricate internal microstructures. In carbon composites, for example, the orientation, distribution, and density of fibers influence mechanical stiffness and failure behavior. In titanium, grain size, porosity, and microcracks can significantly impact fatigue life and biocompatibility. Conventional surface imaging techniques like optical or scanning electron microscopy offer limited insight, as they require destructive sectioning and can only provide two dimensional information. Thus, there is a clear need for volumetric, non-destructive imaging approaches. The objective of this thesis is to evaluate the capabilities of micro-CT imaging in resolving the internal structures of two representative materials, and get information about the structure through the dark-field images even far below the pixel size. Information from other studies is known and can be used to contrast the results from both setups. Through systematic acquisition and analysis of micro-CT and dark-field data, the thesis aims to answer what specific microstructural information can be extracted from each imaging modality, how do the results compare, and whether the micro-CT images and data can be used as a reference for the grating-based phase-contrast setup, answering as well what are the limitations and challenges in measuring these samples.

In this thesis a description of the experimental setup of the micro-CT is given and how alignment was performed in order to correctly calibrate the setup. Then, an analysis of both carbon and titan samples from the projection x-ray images is done. From these projection images, a 3D reconstruction is made, from which structure information is obtained from the samples. After, a directional dependent measurement is done in the grating-based phase-contrast scanner, first explaining how images are filtered, and later analyzed, to obtain information that is contrasted with the obtained data in the micro-CT.

2 Theoretical background

The following chapter aims to introduce the theoretical background for the imaging methods applied in this work. A description of the fundamental properties of X-rays, production methods and their interactions with matter is given. Then, an overview of computed tomography (CT) is shown, focusing on data acquisition, image reconstruction techniques, and potential artifacts, also giving a description of what micro-CT means. Finally the principles of grating based X-ray imaging are presented, including the physical origin and interpretation of attenuation and phase-contrast.

2.1 Fundamentals of X-rays

X-rays are high energy electromagnetic waves consisting of photons with a short wavelength of about 10 to 0.1 $\mathring{A}$. Longer wavelengths are considered to be in the range of extreme ultraviolet (EUV), and shorter wavelengths are generally considered to be in the gamma ray regime. The way X-rays interact with matter is influenced by energy-dependent mechanisms, including photoelectric absorption, Compton scattering, and elastic scattering. Gaining a thorough understanding of these core interactions is crucial for accurately interpreting signal generation in both attenuation-based and grating-based X-ray imaging techniques.

2.1.1 Production and properties of X-rays

X-rays for medical and industrial imaging applications are usually produced with X-ray tubes. The basic principle of an X-ray tube is shown in Fig 1. In these tubes, electrons, emitted by a heated cathode, are accelerated toward a metal target (e.g., tungsten) by a high voltage.

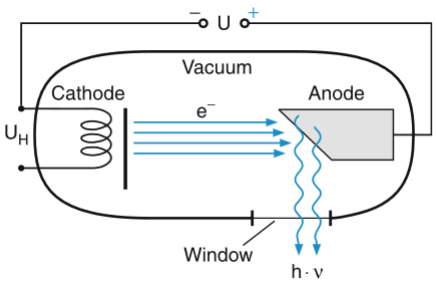

Figure 1: Scheme of an x-ray tube. By a heating voltage U_H, electrons are emitted from the cathode and accelerated towards the anode by a high voltage U_{XRT}. The electrons interact with the anode material, which produces x-rays. These leave the x-ray tube through an exit window. The figure is taken from [11].

Upon reaching the metal target, called anode, the electrons interact with the anode material and photons are emitted via two mechanisms: Bremsstrahlung (braking radiation) and characteristic radiation.

- Bremsstrahlung continuum: Caused by the deflection and deceleration of electrons in the nuclear field converting the energy of these electrons into x-ray photons.

Since, according to electrodynamics, every accelerated or decelerated charge emits radiation with a radiation power proportional to the square of the acceleration, this part of the spectrum is a continuous distribution with energies up to the acceleration voltage. While the maximum photon energy is determined by the acceleration voltage, the overall spectral intensity scales proportionally with the number of electrons, which is determined by the heating current of the filament.

- Characteristic radiation: Arises when an incident electron ejects an inner-shell electron (e.g., from the K-shell) from a target atom and the energy state is then filled by an higher energy electron. The spectral lines of the characteristic X-ray radiation appear only if the energy of the electrons, incident on the anode, is sufficiently high to excite atomic inner shell electrons into higher unoccupied levels. An outer-shell electron then fills this vacancy, releasing a photon with energy equal to the difference between the two electron shells' binding energies, producing discrete emission lines. These lines are unique to the target material [22]. The emitted spectral lines are labeled according to the shell in which the vacancy occurred (e.g., K or L) and the transition path (e.g., α, β).

Different types of tubes can be used, where typical voltages range between 10 keV and 200 keV. A schematic X-ray spectrum combining both bremsstrahlung and characteristic radiation for a tungsten anode is shown in Figure 2. One can see the continuous spectra as well as some characteristic peaks of the tube's material.

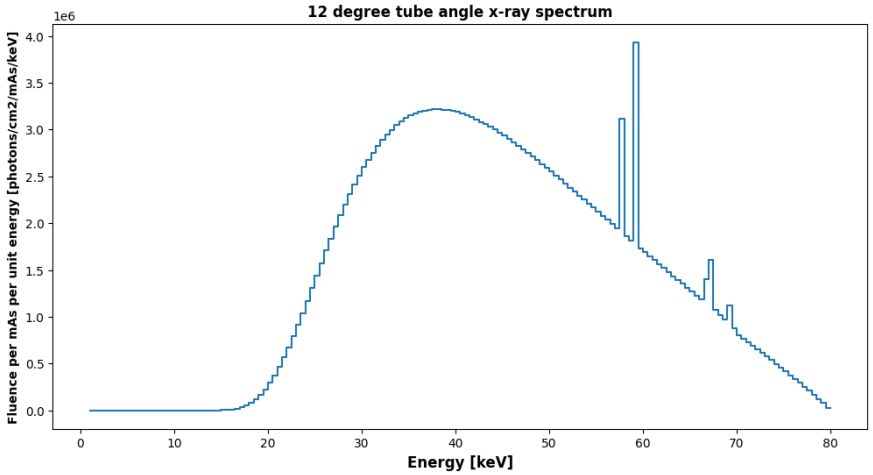

Figure 2: Sketch of the fluence of X-ray emission over the photon energy in keV created by an X-ray tube using 80 kVp acceleration voltage and a tugnsten anode. Several peaks are seen on the right side of the spectrum, related to the characteristic peaks of Tungsten. Plot created using [25].

2.1.2 Focal spot size

Another parameter that is very relevant for this work when discussing X-ray production is the focal spot size of the source. Geometric unsharpness or blur refers to the loss of definition that is the result of geometric factors of the radiographic equipment and

setup. It occurs because the radiation does not originate from a single point but emitted over an area. When we examine the images below, which depict two sources of different sizes, we can observe the paths of radiation from each edge of the source to each edge of the sample feature, the areas of the film exposed by this radiation, and the resulting density profile across the film. The partially shaded region on the edge of the shadow in an image, which is normally referred to as penumbra, is shown in red [23].

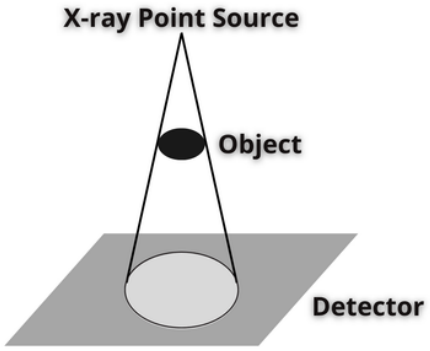

Figure 3: Sketch of the X-ray coverage on a detector shown with a X-ray point source. No blur is seen.

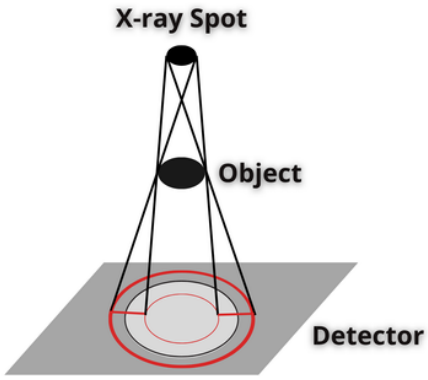

Figure 4: Sketch of the X-ray coverage on a detector shown with a X-ray spot of some quantifiable size. Red lines joining the inside and outside of the oval show the size of the blur.

In the first image, the radiation originates at a point source. Since all of the radiation originates from basically the same point, very little geometric unsharpness is produced in the image. In this case, the penumbra (illustrated by the thin black line on the edge of the X-ray image on the detector) is nearly nonexistent. In the second image, the X-rays are generated in a focal spot with some real diameter, not an ideal point source. In this case, we can see (illustrated by the red lines on the detector) the penumbra is quite a bit larger than with the point source. This is due to the fact that X-rays from all areas of the spot are hitting the edge of the object at slightly different angles, causing partial shading in the detector image. Depending on the setup geometry, this effect limits the resolution to values worse than the detector resolution. In the case of micro-CT this effect can be of big importance. The blur can be expressed as:

$$U = S_{source} \cdot \frac{d_d}{d_o} \tag{1}$$

where U is geometric unsharpness (blur) on the detector, S_{source} is the size of the X-ray source spot, d_o is the distance from the X-ray source to the object and d_d the distance from the object to the detector. For a micro-CT, we want d_0 values to be very small, and d_d values to be big, in comparison, in order to achieve a big magnification. This is why a small source is key in order to be able to see a clear image, because if not, we would obtain a lot of blur. Detector components can also affect this geometric unsharpness.

2.1.3 Interaction of X-rays with Matter

X-rays interact with matter through discrete energy-transfer mechanisms that cause attenuation (reduction in intensity) of the incident beam. These interactions depend on the X-ray photon energy and the atomic number (Z) of the material, and determine how much of the incident X-ray beam is transmitted, scattered, or absorbed. The four ways electromagnetic radiation can interact with matter are: coherent scattering, Photoelectric effect, Compton scattering, and pair production. All of them will be discussed in this section, apart from pair production, which has very high energies which are not relevant to this work. The descriptions are based on [11] and [8].

The total attenuation of an X-ray beam passing through a material of thickness z can be described by an exponential attenuation law, the Beer–Lambert law:

$$I(z) = I_0(-\mu(\lambda) \cdot z) \tag{2}$$

where I_0 is the initial intensity, $I(z)$ the transmitted intensity, and $\mu(\lambda)$ the wavelength-dependent linear attenuation coefficient. This coefficient summarizes the contributions of all interaction processes at the given photon energy. While photoelectric absorption dominates at low photon energies and for high-Z materials, Compton scattering becomes increasingly relevant at higher energies. Elastic Rayleigh scattering, although generally weak, plays a role at low energies and in low-Z materials. At even higher photon energies above 1.022 MeV electron–positron pair production start to happen, however it is not relevant for this experiment.

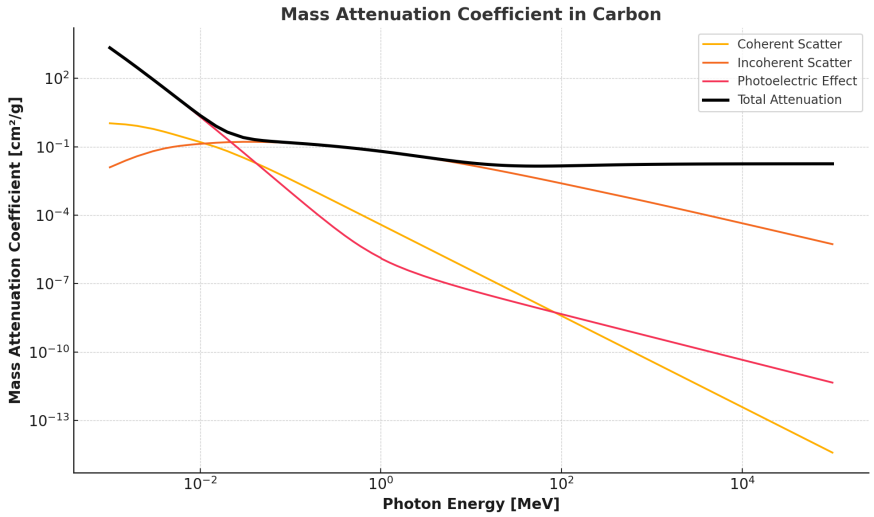

Figure 5: Mass attenuation coefficient and its components for photons in carbon as a function of photon energy. The contributions of photoelectric effect, Compton scattering (Incoherent scatter), and Rayleigh scattering (Coherent scattering) are shown separately. Data taken from NIST webpage [15].

Figure 5 illustrates the energy dependence of the mass attenuation coefficient, which characterizes how easily a mass of material can be penetrated by a beam of light, sound, particles, or other energy or matter [2], and all of its components in a carbon sample.

Rayleigh scattering
Rayleigh scattering is also known as Coherent scattering. It takes place between a photon and an entire atom. No electrons are released from the atom, and no energy is transferred during this process. Therefore the photon only changes its direction but keeps the same energy. It is a so called elastic scattering process.

Photoelectric effect
Photons with energies higher than the binding energy of the atom can be absorbed entirely by an inner shell electron in a process called photoelectric absorption. During this process, the atom is ionized and an electron, which receives all the absorbed energy, is freed. Any energy exceeding the binding energy is transferred to the electron as kinetic energy.

$$E_{kin} = hv - W_{metal} \tag{3}$$

Where h is Planck's constant, v the frequency of the incoming photon and W_{metal} the work function of the metal. The vacancy left by the electron can be filled by an outer shell electron under the emission of characteristic radiation. The cross-section of the photoelectric effect is given by:

$$\sigma_{photo} \propto Z^5/E_\gamma^{3.5} \tag{4}$$

where Z is the atomic number and E_γ the photon energy. Due to the discrete nature of ionisation energies, the cross-section of the photoelectric effect contains sharp absorption edges, where the photon energy surpasses the energy required to remove an electron from an inner shell. The photoelectric effect is especially dominant for materials with high atomic numbers and falls off quickly with increasing energy. This strong dependence on atomic number allows for a good differentiation between bone-like material ($Z_{Ca} = 20$) and the surrounding soft tissue (Z $\approx$ 7) in X-ray imaging.

Compton scattering
Compton scattering is also known as Incoherent scattering. An X-ray photon with energy h sometimes collides with a quasi-free electron. The X-ray photon loses only a part of its energy during the Compton collision. Thus, the scattered photon is of lower energy when it continues its travel through the matter. The energy level of the scattered photon can be measured under the scatter angle θ, via the shift of wavelength:

$$\Delta\lambda = \frac{h}{m_e c}(1 - cos(\theta)) \tag{5}$$

were here m_e is the electron mass and c the speed of light in vacuum. The change of the wavelength does not depend on the initial energy of the photon but only on the scattering angle. Considering the scattering angle θ, at small angles, the energy loss of the photon is minimal, whereas at larger angles (up to complete backward scattering: θ = 180°, where this is maximum) the photon loses significantly more energy. One can rewrite equation 5 as:

$$E' = \frac{E}{1 + \frac{E}{m_e c^2}(1 - \cos\theta)} \tag{6}$$

2.1.4 Detection of X-rays

In order to use X-rays for imaging purposes, spatially resolved detection of X-ray photons is required, and will be explained in this section, mainly referencing [8]. Since the main interaction principles between X-ray photons and matter have been explained in the section above, no new effects have to be introduced to explain the interaction between X-ray radiation and the detector material. Today, almost all modern CT systems are equipped with scintillator detectors. Such a detector essentially consists of two main components: A scintillator medium and a photon detector. When ionizing radiation, such as X-rays, enter the scintillator material, it converts the X-rays into photons of different wavelengths, commonly visible light. The amount and intensity of the emitted light are proportional to the energy deposited by the radiation, so, in a first step, the short-wave X-ray radiation entering the detector is converted into long-wave radiation (light) inside the scintillation media. Then, the emitted light is detected by a pixelated sensor, such as a CMOS or CCD.

2.2 Computed Tomography

In this section, an overview of Computed Tomography will be given, how an image is reconstructed from raw data, and, the importance of micro-CT for this thesis. Most of this work is extracted from [8].

Computed Tomography (CT) is an imaging modality widely used for the visualization of internal structures. Unlike conventional radiography, which projects a two dimensional image of a three dimensional object, taking away one dimension, CT reconstructs cross-sectional images by acquiring multiple X-ray measurements from different angles around the sample. Rays are collected in sets called projections. These projections are then computationally combined using reconstruction algorithms such as filtered back projection or iterative methods to generate volumetric data. This section aims to provide an overview of the data acquisition process and reconstruction techniques.

Angular Range
It is possible to rotate source and detector or to rotate the sample. In the experimental setup used for this thesis the sample itself is mounted on a rotational stage, while the source and detector remain fixed. This arrangement is especially well suited for compact laboratory based setups, as it simplifies the mechanical structure. To achieve accurate image reconstruction, the system must collect projections over a minimum angular range of 180° , ensuring that every region of the object is adequately sampled. This is due to the fact that collecting projections over 180° is mathematically sufficient to reconstruct a cross-sectional image. Each ray path through the object at an angle θ has a corresponding, but mirrored, path at $\theta + 180°$, containing (essentially) the same information. Doing this can reduce scan time. However, it is even better to sample over 360°, as collecting projections over a full 360° can help reduce reconstruction artifacts, especially for objects that contain high contrast features or are inhomogeneous. This is because the additional angular data helps to fill in gaps and correct for inconsistencies that may arise from limited angle sampling. For samples with complex shapes or varying composition, 360° scanning ensures that all features are adequately captured from every possible direction, leading to more accurate and reliable reconstructions. Reconstruction

software is often optimized to reconstruct sample which are rotated fully, which is why the samples in this thesis were always probed a full 360°.

Rotation Step
Another one of the important parameters to select when starting a CT scan is the rotation step. This rotation step (in degrees) will determine how many projections are acquired over 360 degrees of sample rotation. Choosing a rotation step that is too large will result in undersampling, causing images with a lot of noise and artifacts, due to an insufficient number of projections. Choosing a rotation step that is too small will result in long scan times, enhancing the possibility of errors due to source instability. [7] determines that for a detector size of around 2000x2000 pixels a rotation step of 0,15°-0,2° degrees can be taken optimally. In our measurements a rotational step in the range of 0,2° and 0,5° resulted in good spatial resolution while keeping the integration times short enough.

Image Correction
Flat-field correction is essential for achieving accurate quantitative imaging in computed tomography, as it compensates for both global and local detector inhomogeneities. This is done by taking a flat-field image, without any objects shown on the detector, as well as an image when the x-ray tube is off, normally called offset. From there, the offset is subtracted from the flatfield image and its projections, as well as the measurements with the objects, and after, the images with the objects are divided by the reference image. This correction is later applied to all the projection images in the micro-CT setup obtained in this thesis. These images are commonly used to reference samples, before performing more advanced experiments, for example, in grating based X-ray phase-contrast imaging, and to reference the attenuation and dark-field signal in those setups [21]. Comparison between these reference images and the grating-based setup ones, which will be explained later, can yield a lot of information on the way the setups work and a great understanding on the characteristics of the sample, and is one of the resarch topics of this thesis.

2.2.1 CT Image Reconstruction

Practical reconstruction algorithms have been developed to implement the process of reconstruction of a three-dimensional object from its projections. These algorithms are designed largely based on the mathematics of the Radon transform, statistical knowledge of the data acquisition process and geometry of the data imaging system [19]. An overview of the reconstruction process, which will be used in order to obtain the 3D pictures of the samples from the projection x-ray images, is explained in this section, mainly extracted from [18] and [31].

Once all projections are obtained, they have to be processed to be able to reconstruct a 3 dimensional image. CT image reconstruction refers to the mathematical transformation of raw X-ray projection data, captured from various angles around the sample, into detailed cross-sectional images. This process relies on a sequence of critical steps and advanced algorithms to obtain good spatial resolution and signal to noise ratios images. The raw projection data acquired in CT are commonly visualized in the form of a

sinogram. A sinogram represents the signal recorded by a single detector row over a range of projection angles. Each row corresponds to a specific rotation angle of the X-ray source, while each column reflects a detector element. The resulting image shows how the intensity measured at each detector pixel changes as the system rotates, as illustrated in Figure 6.

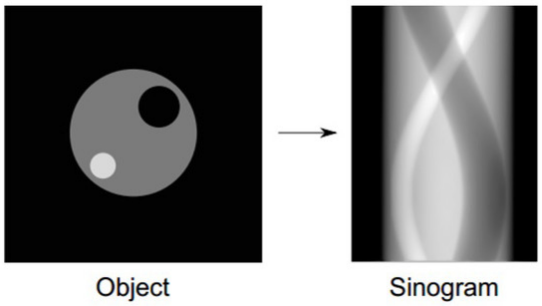

Figure 6: Illustration of how a simple object's projection data is represented in a sinogram. In some cases, the sinogram may be rotated by 90 degrees, which interchanges the horizontal and vertical axes. High-attenuation structures such as bone appear as bright regions, while soft tissues appear darker. Image taken from: [6]

If the measured intensities I have been normalized to a flat-field image I_0, the values correspond to the transmission $T = I/I_0$. A single point in the object produces a sinusoidal trace across the sinogram due to the changing projection angle, giving rise to the name "sinogram". Artifacts like detector defects manifest as distortions in the sinogram, which propagate into the reconstructed image. The sinogram data mathematically corresponds to the Radon transform of the object f(x, y), and can be thought of as the graphical representation of the Radon transform. Introduced by Johann Radon in 1917 [26], the transform describes how projections, the line integrals of the object's attenuation values, are collected at different angles. If $f(x, y)$ is the object, the Radon transform $\mathcal{R}f(s, \theta)$ gives the projection at angle θ and distance s from origin:

$$\mathcal{R}f(\theta, s) = \int_{-\infty}^{\infty} f(s\cos\theta - t\sin\theta,\ s\sin\theta + t\cos\theta)\, dt \tag{7}$$

The mathematical problem of recreating a 2D image from a series of line integrals is complex, but essentially, the problem here lies in inverting this sinogram, meaning, this Radon transform. We will discuss how we can do that in the following.

Fourier Slice Theorem

To invert our raw data projections we can use the Fourier Slice Theorem. The 1D Fourier transform of a projection at angle θ equals a slice through the 2D Fourier transform of the object at the same angle [30].

$$F_s\left\{Rf(\theta, s)\right\} = F_{x,y}\left\{f(x, y)\right\} \tag{8}$$

Basically, what we are doing can be seen in Figure 7 and Figure 8. We are taking 1D slices of the sinogram and converting them into slices of the 2D image of the sample in frequency space. This is also called Central Section theorem, as the 1D slice transforms

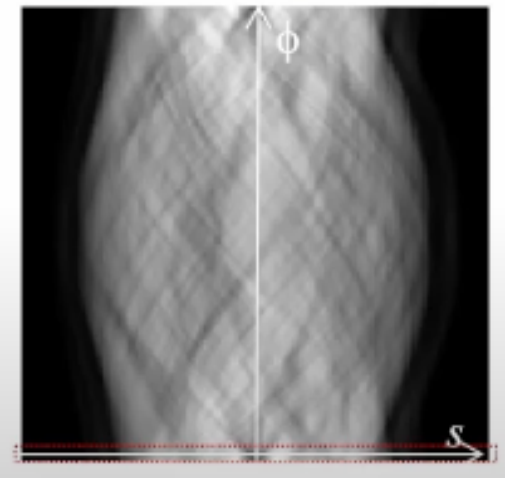

Figure 7: Sinogram of a certain x-ray projection. A slice for a certain angle ϕ is seen surrounded in small red dots. Equation 8 can be applied to obtain the 2D image seen in Figure 8.

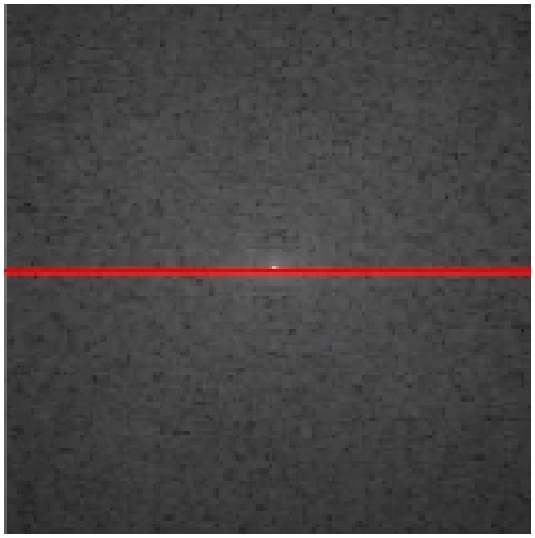

Figure 8: 2D image in frequency space (Fourier transform of the sample's image) obtained by taking the Fourier transform of the 1D slice (in red dots) in Figure 7 leading to the red slice in this figure. This process is done for all angles.

always into a slice that goes through the center of the image, however, for each angle this slice rotates. By collecting projections from multiple angles, the entire frequency space can be filled, allowing the reconstruction of the original image. Now we have obtained a 2D slice image of our sample (we can picture this as having slices of our sample from the bottom to the top in the z axis). Since low frequencies are inherently overrepresented in this process, filtering becomes necessary to restore a balanced frequency response.

Filtering

Filtering corrects the overemphasized frequency components present by amplifying high frequencies. Figure 9 (e/bottom) shows how the unfiltered backprojections show a blur, precisely because of this uneven consideration of frequencies. Each projection is filtered with a special kernel, typically a ramp filter. Often, filtering is performed in the frequency domain by multiplying the Fourier transform of each projection by the filter, then applying the inverse Fourier transform to return to spatial domain. This process is called (filtered) backprojection.

$$Filtered\ Projection = F^{-1}[|w| * F\{Rf(\theta, s)\}] \tag{9}$$

Feldkamp David Kress

In the case of this thesis the classical filtered backprojection (FBP) is not used, but the FDK (Feldkamp Davis Kress) algorithm for the reconstruction, which is an extension of the FBP, that applies a special filter in the frequency domain before back-projecting the projection images. Instead of using plane beam geometry it is made for cone beam geometry. The formula is approximate but has useful properties, including errors that are relatively small in many practical instances and a form that leads to convenient

computation. [13].

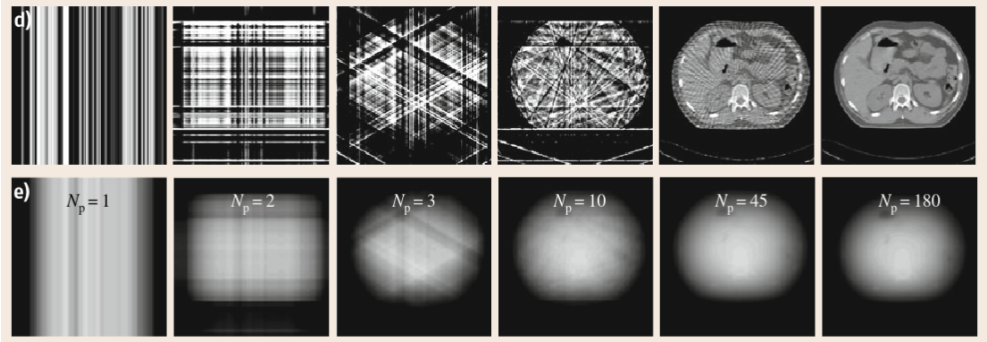

Figure 9: Accumulation of all backprojections of the high-pass filtered (d/top) and unfiltered (e/bottom) projection profiles for different numbers of projections N_p. From left to right: $N_p = 2$, 3, 10, 45, 180. Image taken from [30].

2.2.2 Micro-CT

Micro-computed tomography (micro-CT) is a version of CT, that allows the non-destructive analysis of the 3D structural properties of small objects. Samples can be imaged with pixel sizes as small as 100 nanometers and objects can be scanned as large as 200 millimeters in diameter [9]. The first X-ray microtomography system was conceived and built by Jim Elliott in the early 1980s. The first published X-ray microtomographic images were reconstructed slices of a small tropical snail, with pixel size about 50 micrometers [20]. Micro-CT enables detailed examination of the internal structures of both material and biological samples without the need for physical sectioning, thereby preserving the integrity of specimens or samples for future analysis. The quantitative data derived from micro-CT is inherently three dimensional and cannot be replicated using 2D imaging methods. Thanks to these capabilities, micro-CT is a very valuable tool for analyzing sample morphology and investigating characteristics such as porosity, bone or structural thickness, volume fraction, defects, density, particle size, voids, and fiber orientation, which is the direct cause of the topic of this thesis. It is widely used across disciplines to study a range of subjects including bone, teeth, soft tissues and organs, composite materials, medical devices, batteries, and more.

The working principle is almost the same as the conventional CT mentioned for experimental setups. X-rays are generated in an X-ray source, and end up in a detector after going through the sample probed. Rotation of the sample and image acquisition is the same as in conventional CT imaging.

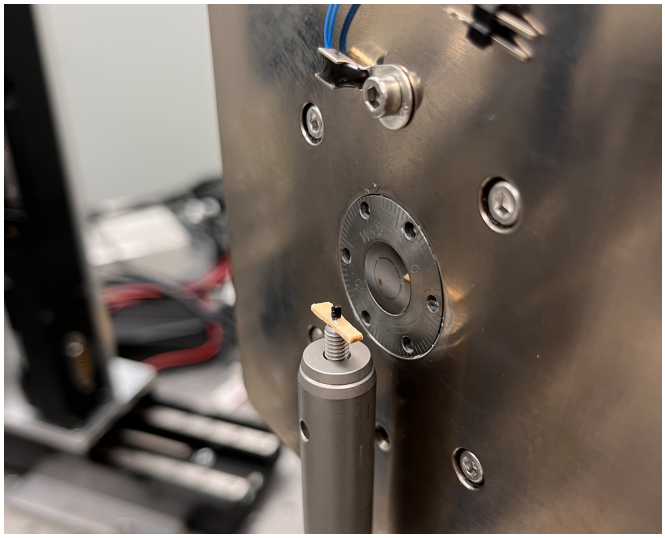

Figure 10: Experimental setup of micro-CT, with carbon sample (small black chunk) glued to a wooden base, mounted on the rotational stage. The black circular aperture contains the x-ray source.

Instead of using very small pixel sizes, the object is magnified by placing it closer to the X-ray source, which increases the effective resolution on the detector. In this setup, the magnification of the sample can be calculated taking the distance from detector to source, X_{dts}, and dividing it by the distance from sample to source, x_{sts}.

$$magnification = \frac{X_{dts}}{x_{sts}} \tag{10}$$

This magnification effectively enlarges the projected image of the object on the detector, allowing for features to be resolved more accurately without the need for physically smaller detector pixels. However, increased magnification also amplifies the effects of blur, as seen in Equation 2.1.2. That is why, high-resolution micro-CT systems often require an extremely small X-ray focal spot (in the micron or sub-micron range) to maintain image sharpness at high magnifications. This trade-off between magnification, source size, and image sharpness is a critical consideration in micro-CT system design. Sample size also needs to be small (material needs to be manageable at those very small sizes) in order to achieve a big magnification within the entire field of view of the detector, otherwise artifacts emerge. In a big sample, the distance from source to the object must be increased in order to image the entire sample, leading to a lower magnification. In Figure 10 sample is 7 mm away, while the detector is 310 mm away from the source, which allows for a magnification of more than 44. Such a small sample allows an even further decrease in distance to the source. As we will see in the following chapter, the setup of a rotational stage that correctly rotates and is aligned with the source is key in such small distances, as the sample can easily go away from the detector's sight.

2.3 Grating based X-ray Phase-Contrast imaging

In this section the X-ray wave propagation and complex refractive index are introduced in order to describe how X-rays interact with matter on a microscopic level. This will allow to explain how phase shift is generated and give an overall overview of the effects this causes, and how this is used to obtain additional information in these grating based setups.

2.3.1 Complex Refractive Index of X-rays

Following section is extracted from [24]. The propagation of X-rays through a medium is governed by the wave equation, which, assuming a linear responding material like most dielectric materials, with refractive index n, takes the form:

$$\left(\frac{n^2}{c^2}\frac{d^2}{dt^2} - \Delta^2\right)\Psi = 0 \tag{11}$$

For X-rays, the refractive index n_w is generally a complex number that deviates only slightly from unity and can be written as:

$$n_w = 1 - \delta_w + i\beta_w \tag{12}$$

For a wave propagation in z-direction through an object with a refractive index n_w, wave equations can be solved using a plane wave, assuming a monochromatic wave with angular frequency ω, of the form:

$$\Psi(\mathbf{r}, t) = \Psi_0 e^{i(\mathbf{k}\cdot\mathbf{r} - \omega t)} \tag{13}$$

The wave vector $\mathbf{k}$ is then modified according to:

$$\mathbf{k} = |\mathbf{k}_0| = k_0\left(1 - \delta_w + i\beta_w\right) \tag{14}$$

where $k_0 = |\mathbf{k}_0| = 2\pi/\lambda_0$ is the vacuum wave number, and λ_0 the vacuum wavelength. Assuming wave propagation only in the z-direction, the wave vector simplifies to $\mathbf{k} = k_z\hat{z}$, where the z-component is given by $k_z = k_0 n$. Therefore:

$$\mathbf{k}\cdot\mathbf{r} = k_0 n z = k_0 z\left(1 - \delta_w + i\beta_w\right) \tag{15}$$

This leads to a modified wave equation:

$$\Psi(z, t) = \Psi_0 \exp\left(ik_0 z(1 - \delta_w + i\beta_w) - i\omega t\right) \tag{16}$$

$$\Psi(z, t) = \Psi_0 \cdot \underbrace{\exp\left(ik_0 z - i\omega t\right)}_{vacuumpropagation} \cdot \underbrace{\exp\left(-ik_0\delta_w z\right)}_{phaseshift} \cdot \underbrace{\exp\left(-\beta_w k_0 z\right)}_{attenuation} \tag{17}$$

The first term in Equation 17 represents the vacuum propagation of the wave. The third term accounts for the attenuation of an X-ray beam as it passes through matter, which is similar to the description of the Beer-Lambert law in Equation 2. The second term is a phase factor that captures the shift in the phase oscillation, given by $ik\delta_w z$, due to the presence of the material. This effect can be seen visually in Figure 11. Measuring only the intensity of a wave, the second term is lost and the phase shift cannot be measured. Using a grating based setup, this phase shift can be measured.

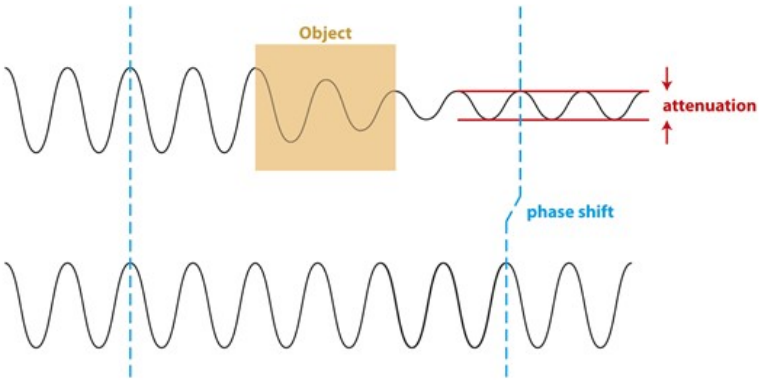

Figure 11: Illustration of the effect of a complex refractive index on an X-ray wave. Absorption leads to attenuation (red), while refraction causes a phase shift (blue). The lower wave shows the unmodified reference. Image taken from [3]

2.3.2 Talbot Interferometry

Phase shifts cannot be measured directly. Instead, interference phenomenons are used to indirectly measure the influence of the phase shift on the wave field. On the basis of the Talbot effect a grating-based X-ray Talbot interferometer can be designed, which consists of two gratings: a phase grating (G1) and an analyzer grating (G2). Together, they form an interference pattern that is sensitive to both phase shifts and small-angle scattering in the sample. Hence, the full information of the complex refractive index (Equation 12) is accessible by X-ray Talbot imaging. Most of the following overview is extracted from [21].

Talbot Effect
The Talbot effect is an interference phenomenon, in which a periodic structure creates images of itself at certain distances, known as Talbot distances, behind the structure when under coherent illumination. For a plane monochromatic wave and absorption gratings, the Talbot-distances are [24]:

$$d_t^m = \frac{mp^2}{\lambda} \tag{18}$$

where m is an integer, λ the wavelength of the incident light and p the period of the grating. This works for absorption gratings, but also for phase gratings which absorb very little X-rays but module a periodic pattern onto the phase front of an incident wave. The phase shift depends on the grating height and the photon energy. Absorption gratings are fabricated in the regime of elements with a high atomic number to achieve high absorption with a reasonable grating height. Phase gratings, however, are fabricated from elements with low atomic number, e.g. photo resists, ideally to induce only a phase shift. Common designs include π and $\pi/2$-shifting gratings. Absorption gratings primarily block transmission at the grating bar locations. The grating's duty cycle $D_c = w/p$, defined as the ratio of gap width w to period p, is typically set to 0.5 to maximize fringe contrast. High contrast interference fringes suitable for image signal extraction only form at specific fractional Talbot distances d_{fT} , which depend on the grating design. At full Talbot distances d_T , the self-image of the phase grating is

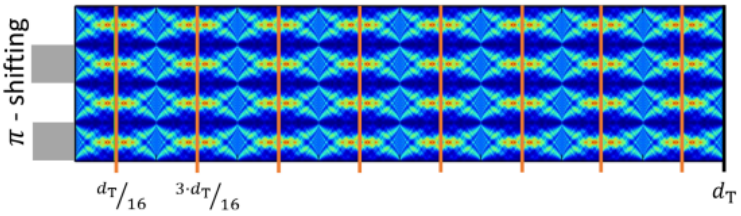

Figure 12: Simulated Talbot carpet for a π-shifting phase grating under monochromatic plane wave illumination. The image shows the intensity distribution along the propagation direction. At specific fractional Talbot distances, marked by orange lines, high-contrast lateral fringe patterns appear due to near-field interference. The frequency doubling effect, characteristic of π-shifting gratings, is also visible. Image taken from [14].

laterally uniform and does not produce a measurable modulation in intensity. For a π-shifting grating, usable self-images appear at distances:

$$d_T = \frac{2m-1}{16} \cdot d_{T1}, \quad m \in \mathbb{N}. \tag{19}$$

where d_{T1} is the first Talbot distance. This configuration leads to a spatial frequency doubling of the fringe pattern and allows higher fringe resolution downstream. A simulated Talbot carpet illustrating this effect is shown in Figure 12.

To capture this fine interference pattern, the analyzer grating G2 is positioned exactly at such a fractional Talbot distance d_{fT} downstream of G1. G2 is an absorption grating that acts as a sampling mask and enables the indirect detection of the periodic intensity modulation. Its period p_2 is matched to the fringe period p_T at the chosen Talbot plane, allowing the fringe contrast to be measured via the phase-stepping procedure explained in the next subsection. Refraction within the sample leads to a lateral shift of the fringes, while small-angle scattering causes a local reduction in fringe visibility. In real systems, several effects such as the finite source size and poly-chromaticity of the X-ray beam degrade fringe visibility. The resulting fringe pattern is a superposition of multiple overlapping Talbot carpets for different wavelengths, as illustrated in [21]. Therefore, the exact placement of G2 is chosen to maximize fringe visibility.

Lau effect

Since the Talbot effect relies on interference, achieving high spatial coherence from the source is also essential. This can be achieved by using a sufficiently small source. When using such a source, the X-rays are emitted in a cone beam geometry, causing the Talbot pattern to magnify as the distance from the focal spot increases. Conventional X-ray tubes produce spatially incoherent radiation. To enable interference under such conditions, the so-called Lau effect is exploited: a source grating G0 subdivides the broad beam into an array of narrow, mutually coherent beamlets. Each of these beamlets can form its own Talbot pattern downstream. Without G0, the patterns from the extended source would superimpose incoherently, and the interference signal would vanish. Setup of a Talbot-Lau interferometer can be seen in Figure 13.

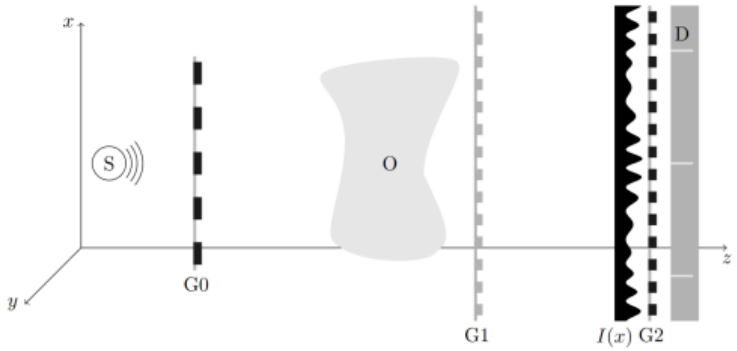

Figure 13: Schematic of a grating-based X-ray Talbot-Lau interferometer with source (S), gratings G0–G2, sample (O), and detector (D). Image taken from [28].

2.3.3 Phase stepping

The Talbot pattern is usually too small to be resolved so the grating G2, an analyzer grating, is introduced to sample the pattern in the Phase stepping scheme. To sample the Talbot pattern, the movement of the sample is replaced by the movement of the gratings, so, the G2 grating is shifted along the Talbot fringes within at least one grating period $p2$. The grating is moved in several equidistant steps in fractions of one grating period of G2. For each so called phase-step one image is acquired. In this work, the source grating G0 was moved, which is mathematically equivalent to stepping G2, as only the relative phase between the interference pattern and the analyzer grating is relevant. The measured intensity values are plotted as a function of the phase-step position for each pixel. A polychromatic extended X-ray source leads to a blurring of the Talbot pattern and consequently blurs the phase-stepping curve to a sinusoidal curve. The described phase-stepping procedure is performed once with the object (object measurement) and once without the object (reference measurement). The parameters of the two phase-stepping curves contain per pixel information about the contrast and position of the underlying Talbot pattern.

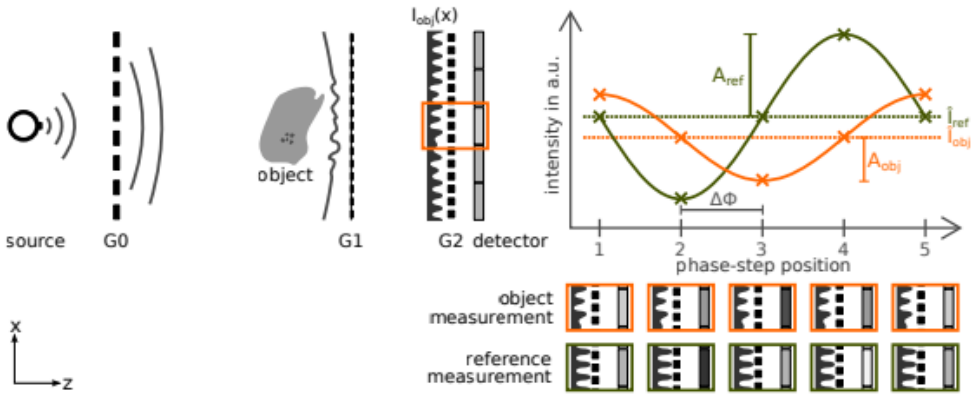

Figure 14: Principle of phase-stepping procedure: The analyser grating G2 is shifted along the intensity pattern in x direction. For each grating position one image is acquired and the resulting intensity values are plotted over the appropriate phase-step positions for every pixel. This process is applied once for a measurement with object and once without which leads to two sinusoidal curves. The images are taken from [21].

By comparing the object scan with a reference scan without the object (often referred to as a flat-field image), the influence of the object onto the wavefront can be reconstructed, and the following three signal modalities can be derived.

2.3.4 Modalities of image acquisition

The change in the phase-stepping curve encodes the information required for retrieving the additional image modalities. A sinusoidal I intensity curve

$$I(x) = A \cdot sin\left(\frac{2\pi x}{p_2} + \Phi\right) + I \tag{20}$$

is fitted to the object (obj) and reference (ref) phase-stepping curves depending on the grating position x respectively phase position $\frac{2\pi x}{p_2}$. With the gained parameters mean intensity I, amplitude A and phase Φ the images can be extracted.

Attenuation Image
The attenuation image is calculated from the mean intensity of the phase-stepping curve. It is defined as the ratio of the mean intensity of the object scan to that of the reference scan:

$$\Gamma = -\ln\left(\frac{I_{\text{obj}}}{I_{\text{ref}}}\right) := \mu. \tag{21}$$

In this form, highly absorbing materials will be seen as areas with values close to zero. Areas where little to no absorption takes place will produce pixel values close to one. In this sense, attenuation image behaves very similarly to the CT absorption images process.

Differential Phase Contrast
The differential phase-contrast (DPC) image is obtained from the phase shift $\Delta\Phi$ between the object and reference phase-stepping curves Figure 14:

$$\Delta\Phi = \Phi_{ref} - \Phi_{obj} \tag{22}$$

This contrast arises due to refraction of X-rays at interfaces within the object, which causes a slight angular deflection of the wavefront and shifts the Talbot pattern recorded by the detector. The DPC image is sensitive to a change in thickness of the object. Areas where no target is present share their differential phase value with areas where a target of constant thickness is present. The edges, where the thickness changes rapidly, produce an easily visible signal within the DPC image.

Darkfield

The dark-field signal arises from ultra-small-angle X-ray scattering (USAXS), where X-rays are scattered by tiny structural variations, such as pores, fibers, or grain boundaries. These features are generally much smaller than the spatial resolution of the imaging system. While they do not cause significant absorption or refraction, they induce slight angular deviations in the wavefront, which locally distort the interference fringes and produce changes in the stepping curve. As a result, dark-field imaging is highly sensitive to microstructures that would otherwise be invisible in traditional attenuation or phase-contrast images. In Talbot-Lau imaging the reference visibility is an important quality parameter. The visibility V can be defined as contrast:

$$V = \frac{I_{max} - I_{min}}{I_{max} + I_{min}} = \frac{A}{I} \tag{23}$$

The dark-field image is then derived from the relative reduction in visibility V of the interference fringes caused by the small-angle scattering within the sample.

$$DF = -log\left(\frac{V_{obj}}{V_{ref}}\right) \tag{24}$$

The dark-field image therefore provides information about how strong the intensity Talbot pattern of the phase grating G1 is disturbed, i.e the contrast of the pattern decreased. The more edges, fibrous or granular structures are located in a sample, the stronger is the dark-field signal. Furthermore, if hardly any attenuation occurs there could nevertheless be a dark-field signal. The mean intensities of reference and object measurement could be similar, while the corresponding amplitudes differ a lot. These characteristics of the dark-field images come to play an important role in this thesis, as we will look at these images searching for such microstructures, comparing them with the images obtained in the micro-CT.

Directional X-ray dark-field imaging

A typical Talbot-Lau interferometer consists of unidirectional gratings. Scattering of an incoming X-ray wavefront at micrometer-sized structures in a sample leads to a local destruction of the wavefront. The Talbot pattern reproduces the unidirectional shape of the grating bars. In consequence, the pattern is only sensitive to the wavefront gradient in the direction perpendicular to the grating bars. Thus, a dark-field signal occurs only for scattering contributions in that direction. The parallel scattering contributions do not have an influence on the shift (differential phase image) or the contrast of the Talbot pattern, seen in Figure 15. This enables a reconstruction of fiber orientations and a degree of anisotropy, usable for further structural analysis.

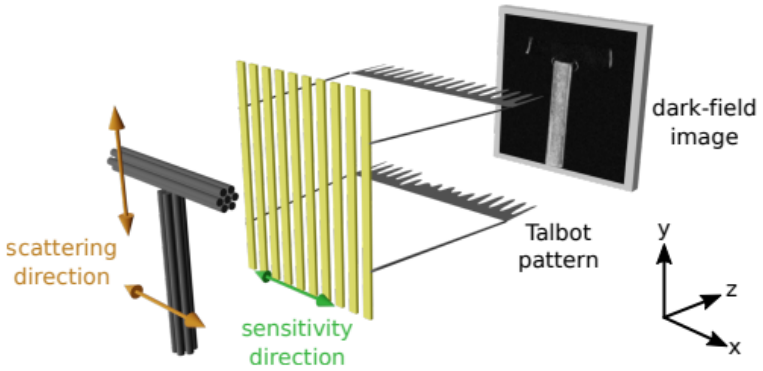

Figure 15: Principle of directional dark-field imaging. Scattering which occurs in sensitivity direction (perpendicular to the grating bars), leads to a measurable change in the contrast of the Talbot pattern (bottom part of fibrous T-shape and edges of top part). In case of scattering which is perpendicular to the sensitivity direction, the Talbot pattern is not reduced in contrast (top part of fibrous T-shape). Image taken from [21].

3 CT Imaging

One of the goals of this thesis is to accurately set up and commission a micro-CT setup. In order to do so, firstly, a description of the experimental tools used in this thesis is given. Then calibration of the micro-CT setup is discussed, as we need to ensure that we are obtaining accurate data. This part is quite important as it directly affects the accuracy and quality of the reconstructed 3D images. This chapter also presents the first experimental data. Finally and overview of the data obtained is given and transmission images are analyzed to extract some general information about the sample that will be useful when the 3D reconstruction is made.

3.1 Micro-CT Experimental Setup

The final micro-CT measurement setup used in this thesis will be explained in this section. A Finetec Feinfocus 160FOMM microfocus X-ray tube is used as an X-ray source [17]. It achieves up to 8 W with source sizes smaller than 5 μm. This source spot size changes with the power applied, with a smaller spot when currents and voltages are decreased, of around $3\mu m$, and growing in size to $5\mu m$, when the voltage and current are increased. The X-rays are detected using a Teledyne dalsa shadobox 6k HS detector, which is a scintillator detector, placed at a distance of 310 mm. The Shad-o-Box HS detectors contain internal shielding to protect the sensor and camera electronics from x-ray radiation. The cameras are optimized for the 40-160 kV energy range, but may be used with x-ray energies as high as 225 kV, and has a pixel size of 49 μm. Some detectors can be equipped with different scintillators in order to optimize their sensitivity and resolution for a given application. In particular, the Shad-o-Box digital x-ray camera can be equipped with different scintillator options at the factory to match a specific energy range or resolution requirement [33]. This is important, because the choice of material is critical, as it depends on the desired quantum efficiency for the conversion from X-ray to light and on the time constant for the conversion process, which determines the afterglow of the detector. The entire metal seen at the right of Figure 17 is the X-ray tube. It is focused onto the circular window, which is called a transmission target, so the source point is directly on this target. The x-ray is precisely located at the edge of the aperture, so we can just measure the distance to the sample and to the detector from the circular aperture. The rotation stage, which can be seen in Figure 16, consists of two linear axes to set the magnification and move the sample in and out of the focus of the detector (allowing to take the reference measurements without manipulating the setup), and a rotational axis to rotate the sample. The axes are mounted onto a groundplate, which contains 3 micrometer screws that allow adjustment of the alignment of the rotational axes. The base of the rotation axis is a thick metallic rod which bumps into the base of the x-ray microfocus tube. In order to be able to get the sampler closer to the source, a thinner rod was manufactured. This was done as other attempts using wooden sticks yielded uneven rotations, making the sample steer out the focus of the setup. Even the manufactured rod had to be scraped on the top and base in order for the rotation to be as accurate as possible, showing the importance of the rotation alignment for this thesis. A slight change in the rotation base yields a clear difference in images. In the following figure the final setup of the micro-CT is shown.

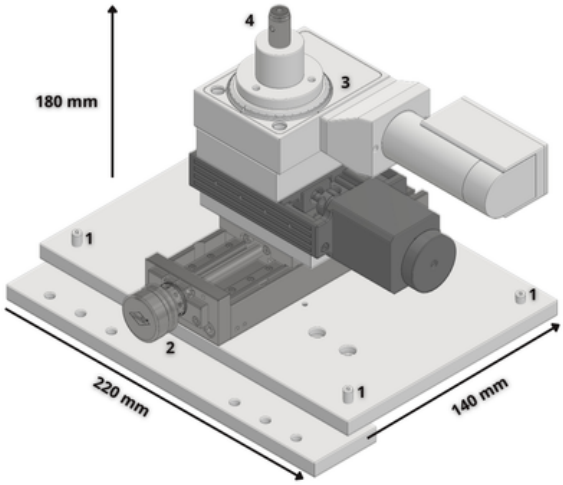

Figure 16: Rotation axis setup. Guide lines are given to show the size of the setup. 1 shows the three screws that allow to adjust the height of the supporting metallic base of the setup (groundplate). 2 shows a circular rotating screw that allows for the axis to be moved closer or further away from the x-ray source, with an accuracy of 0.1 mm. 3 refers to the actual rotation controller, which has a visual rotating scale. Below this, in a darker color, another controller is pictured, which allows lateral movement of the sample to focus in and out of the detector. 4 is the base of the rotating axis, which can be adjusted in height. Here a thin rod can be mounted in order to achieve a big magnification without bumping into the base of the x-ray tube.

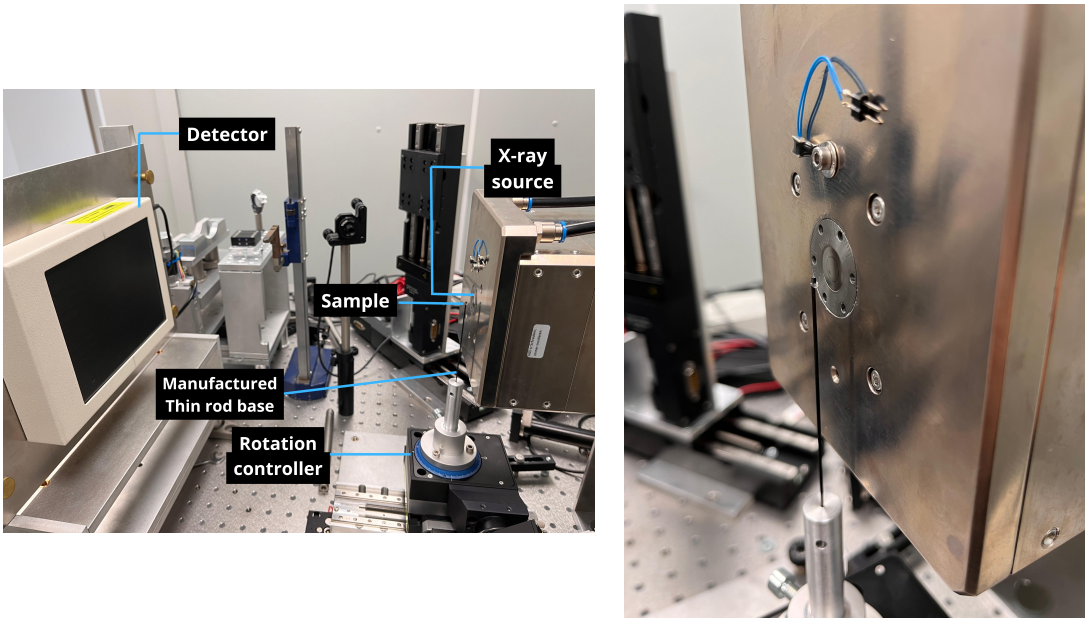

Figure 17: (Left) Complete setup of the micro-CT is shown. At the left side of the image the detector, a black rentangle on a white base is mounted on a metal supporting plate. On the right, the metal encapsulation of the x-ray microfocus tube, distinguished by two tubes at the top. Right below, the rotation axis, sketched in Figure 16, with a black base, and a blue scale that indicates visually the rotation angle. (Right) A closer image at the thin rod used to hold the sample. Typical sample sizes measured in this setup are below 1 mm. X-ray source is right at the edge of the black circle

3.2 Alignment of rotation axis

The mathematical algorithms discussed in section 2.2.1 assume the sample rotates around a fixed and well-aligned axis. If the rotation axis is even slightly misaligned or offset, it can introduce significant distortions in the reconstructed images. Furthermore, working with samples so small, and magnifications so big, a part of the sample not showing at a particular angle of the rotation is very likely. Once calibration is made, the absorption images are looked at, as the base and a first indicator on which structures our sample might have. After the alignment is discussed, flatfield images for both samples will be looked at and analized.

The rotational axis as a whole has to be aligned parallel to the detector plane, as to avoid changing the magnification during rotation and parallel to the pixel columns. To ensure a precise rotational geometry in our CT setup, we implemented an alignment procedure for the rotation axis relative to the detector plane. For this purpose, three small metallic spheres were attached to a thin plastic rod using a small amount of glue, see Figure 18. The spheres were positioned at different vertical heights along the rod. This rod was then fixed into the sample holder, which rotates during scanning, at an angle of approximately 20° from the vertical. Measurements in the x and y axis positions of the spheres were performed in order to align this rotation with the detector plane. This alignment idea was taken from the works of [14], and was refined to further increase the precision.

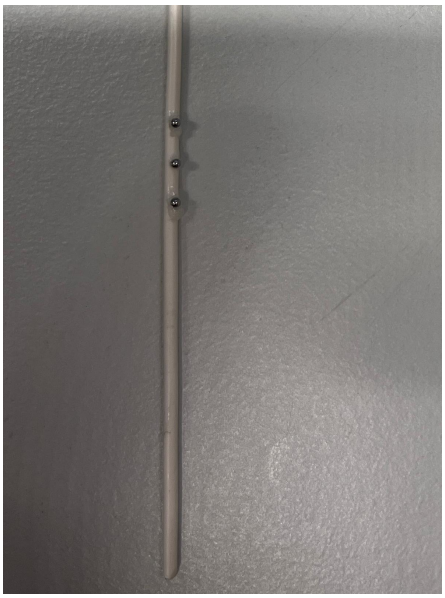

Figure 18: 3 metallic spheres glued to a plastic rod. This configuration was later mounted to the rotational stage, in order to calibrate the alignment of the rotation axis.

Several scans were performed with an X-ray tube voltage of 40 and 80 kV and a current of 200 μA. For each alignment measurement, a total of 72 projection images were acquired, taken with a angular sampling distance of 5°. From these images, the Flat-field correction discussed in subsection 2.2 is applied. From the acquired corrected projection images the positions of the spheres were detected using the center of mass function from the scipy.ndimage package, which provided the (x, y) pixel coordinates of the sphere centers for each angle. For each sphere, the mean and standard deviation of the vertical position (y) were computed. In this direction, the standard deviation of the y values provides a first overview about the position of the X-ray beam center. A sphere placed precisely at the height of the iso ray, defined as the central ray that strikes the detector perpendicularly, will show minimal vertical movement during rotation, and therefore should show a standard deviation of y coordinates of 0. Conversely, spheres located above or below this central ray will display sinusoidal variations in the y-direction, a result of the cone-beam geometry, visually displayed in Figure 19.

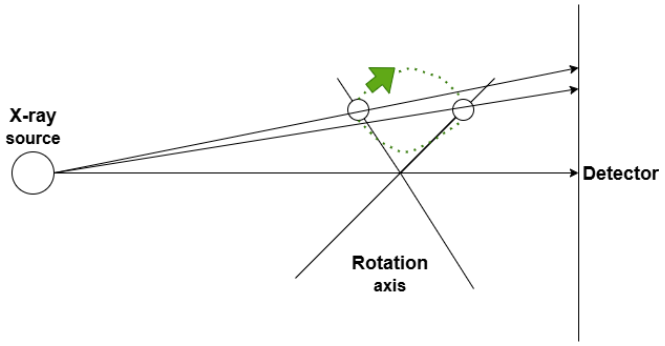

Figure 19: Sketch of how the rotation of a sphere, marked with a green arrow and dots, which is not in the center of the source beam will produce a image with a difference in height in the detector screen.

With this first approach one could determine the height of our beam, in order to set the middle sphere in the precise center of the beam. This is the position we want to set up our sample in.

In the x direction, ideally, if the rotation axis is perfectly aligned perpendicular to the detector, all three spheres should share the same mean x position. Any variation suggests a tilt or misalignment of the axis relative to the detector plane. The horizontal (x) positions were analyzed using a slightly different method. Instead of relying on each individual value determined by the scipy package algorithm, the mean x positions were calculated by averaging pairs of opposing projections, such as scan 1 and scan 37, which are 180° apart. This technique minimizes the effects of projection distortion, as well as poor determination of the spheres center in the python algorithm, and offers a more reliable estimate of the rotation axis's horizontal position within the detector plane, compared to just taking all the x positions of the spheres. The resulting trajectories (see Figure 20 and Figure 21) reveal the circular motion of the beads, enabling visual evaluation of both symmetry and vertical displacement. The statistical values obtained of the movement of the spheres is seen in Table 1.

Sphere	**X: Mean (px)**	**X: Std Err (px)**	**Y: Mean (px)**	**Y: Std Dev (px)**
Sphere 1	1456.51	5.16	225.94	3.93
Sphere 2	1461.47	4.24	866.43	0.32
Sphere 3	1466.37	4.38	1483.48	3.01

Table 1: Summary Statistics for Each Sphere (X and Y mean and standard deviation values), for the detected positions of the three spheres in the alignment setup, with the use of the scipy.ndimage package. Standard error is calculated taking the standard deviation and dividing it by the square root of the number of projections taken.

This alignment idea was the work of [14], however, a further step was taken in this thesis, to try and set up the rotation axis as perfectly as possible. Taken the previous explanation as a first approach, the trajectories of the spheres were analyzed. As they are ellipsoidal, one can estimate the center of the ellipsoidal movement taking the x and y coordinates of the spheres, and averaging the position of pair of opposite coordinates. This gives a set of points, from which one can make a linear fit. This linear fit serves

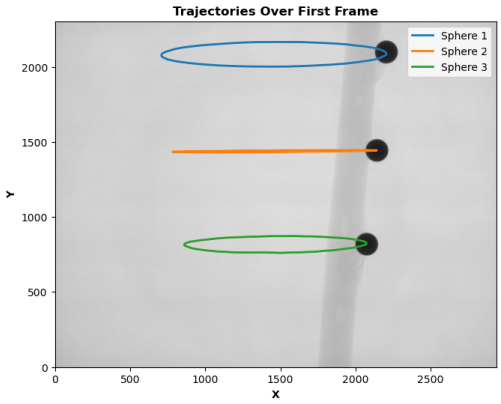

Figure 20: Detected trajectories of the three metal beads over 72 projections. The trace shape provides visual feedback on vertical variation and symmetry, with minimal vertical deviation indicating proximity to the iso-ray.

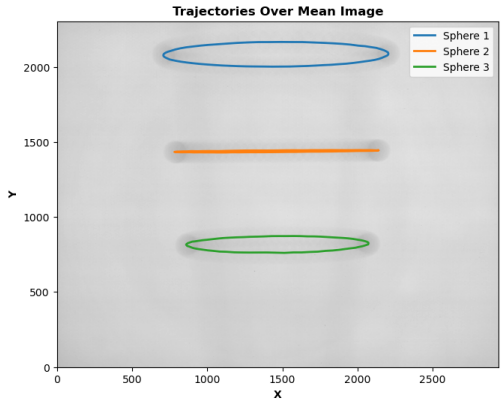

Figure 21: Detected trayectories of the three metal beads with a background image of the mean of the 72 image projections, which gives a visual tool to check the functionality of the scipy.ndimage algorithm.

as a reference line, the semi-major axis of the ellipse that the spheres have, seen in Figure 23 and Table 2. Ideally these lines are perfectly aligned with the detector pixel grid in horizontal direction. However, when tilted, the fit of these lines will give a slope, from which one can extract the deviation angle from the horizontal x axis using the arctangent.

$$angle = tan^{-1}(slope) \tag{25}$$

$$tg(\alpha) = \frac{b}{a} \tag{26}$$

Then, we again use the tangent function to geometrically solve how we need to tilt our detector. This can be more clearly seen in Figure 22. The base of the rotation axis has dimensions of 220x140 mm, which gives us the distance b. Once extracted the angle from the slope obtained using Equation 25, we can obtain a from Equation 26 the distance a, which tells us how much is our rotation base deviated in a certain direction. From here, we need to compensate this height deviation. Screws, shown in Figure 22 as circles, allowed to move in the upwards or downwards direction the base of the rotation axis. Each turn of the screw would yield a height increase or decrease, depending on the direction, of 0.25 mm.

In this case, one would expect to obtain 36 points (pairwise center of 72 coordinates), however the algorithm was not smooth enough to obtain all the points, as it left out the ones who could not correlate well within a certain threshold. However, as one can see visually in Figure 23, this does not pose a problem to obtain the center of the ellipsoids correctly.

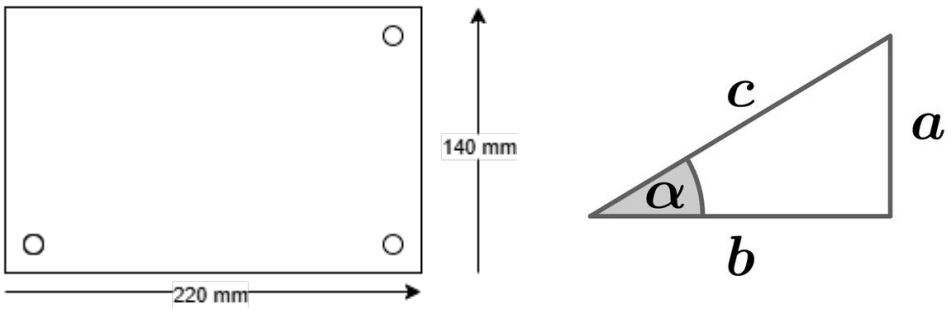

Figure 22: (Left) Sketch of the metallic supporting base of the rotation axis. The 3 screws are here pictured as circles. Distances are shown in order to plug them in for calculations. (Right) Sketch of an angle and the sides of a triangle, to help visualize the deviation in height for a certain angle.

Sphere	**Linear Fit Equation**	R^2
Sphere 1	$x = -0.0076y + 302.67$	0.977
Sphere 2	$x = -0.0103y + 951.40$	0.996
Sphere 3	$x = -0.0112y + 1572.18$	0.968

Table 2: Linear Fit Equations and Coefficients of the linear fit equation for each sphere

From the values in Table 2 one can extract the tilt of the axis setup, which in this measurement case was of -0.59 ± 0.06 degrees. After correcting for this tilt in the setup, the improved determination of the deviation angle reduced the tilt angle to -0.05 ± 0.02 degrees. It is not possible to correct this small value with enough precision (minimal value of 0.06 degrees). If we take a look again at Equation 26 we will see that, introducing the height change of one turn of the screw, this change can only occur with less than a full turn of the screws.

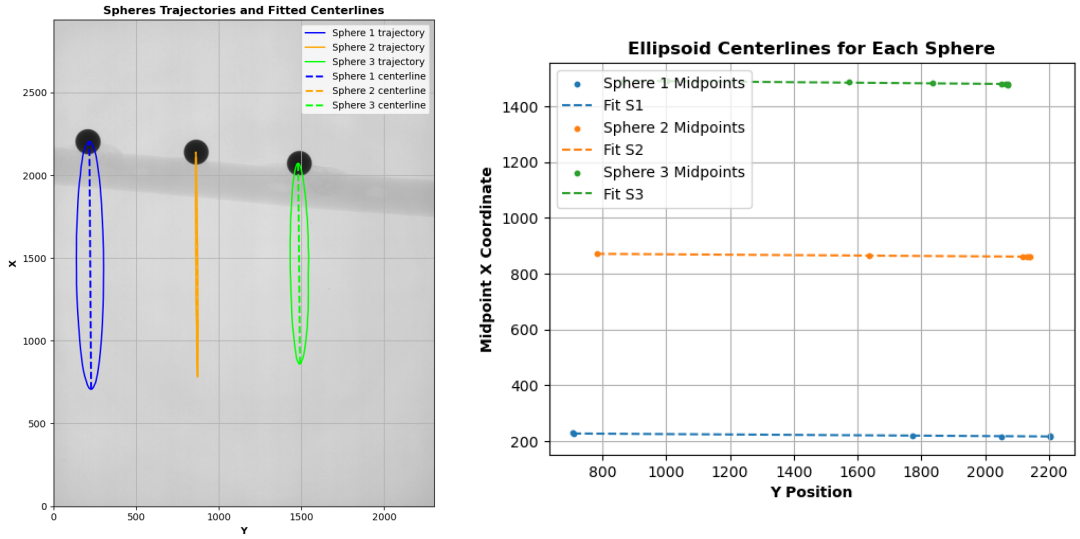

Figure 23: (Left) Lines represent the ellipsoidal movement of the spheres. Dashed lines represent the central line (linear fit) of the ellipsoid formed by the sphere's movement. Axis are rotated in the detector, and not switched on this image, which is why image appears tilted. Highest Y values correspond to the lowest height values in the setup. Highest X values correspond to the left side of the detector, looking at it from the source. (Right) Linear fit of the opposite points obtained from the x-y coordinates of the center of the spheres.

One would think half a turn could yield a better result, however, due to the way the setup is built, a movement in one direction would in turn affect a bit the values in other areas of the base of the rotation, meaning a full turn of the screws was somewhat more precise (one can see in Figure 16, the setup, as well as in Figure 22, that there are only 3 screws, and not 4, meaning one side of the base is more accurately moved than the other). Even a full turn of the screw has a very tiny error. Taking into account the size of our detector (in number of pixels), the pixel size, and this deviation angle, we can estimate a maximum deviation in the image of 100 microns, which would mean we have a maximum deviation of around 2 pixels in a 2940x2304 pixel size detector. This sounds like too much at first, but can be considered a good enough approximation. The scintillator actually worsens the resolution to about 2 pixels [27]. So this is enough to have aligned the rotation axis and to start taking sample measurements.

3.3 Carbon Sample Analysis

The carbon sample is prepared, firstly by taking a very small piece out of it. Full sample, in the case of carbon has a size of 50.3x50.3 mm, and the size of the titan sample, 22.9x22.9 mm, see Figure 24. In the same figure we can in fact see at the corner of the samples, a small piece that's missing, which corresponds to the part taken out. These, due to their large size, cannot be used in the micro-CT setup. These small pieces are taken out of the sample and glued to the rotation base.

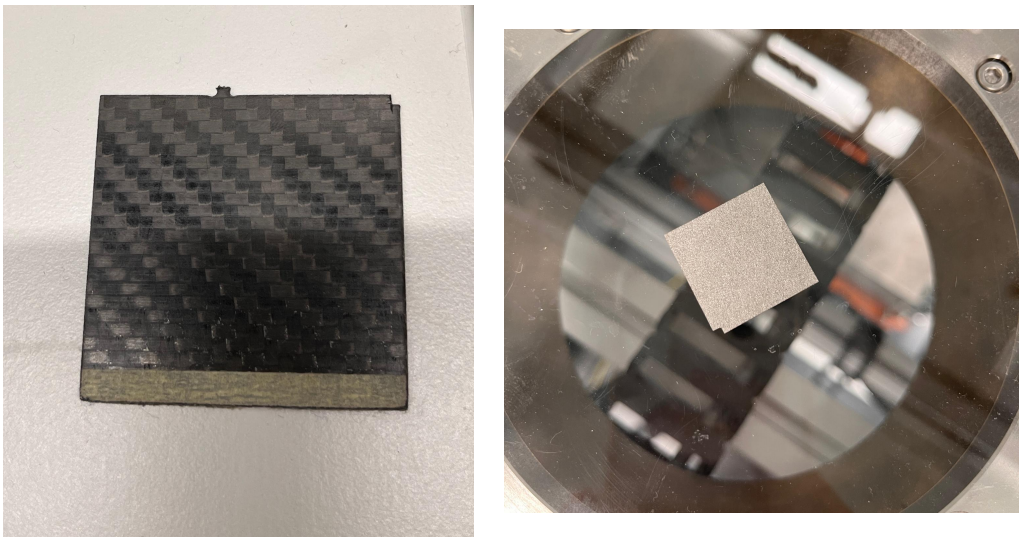

Figure 24: (Left) Image of the full carbon sample. At the top right corner of the sample, the piece that is missing is the one extracted to measure in the micro-CT. (Right) Image of the full titan sample measured in the grating based setup. The small piece extracted can be seen at the bottom corner of the sample.

First images include a wooden base, as this was used to keep the sample from falling down in the metallic rod. This was later not needed when the new manufactured rod was included in the setup. According to the laboratory from which this sample was sent, there are 4 layers of fibers within the 1mm thickness of the sample, where some layers have a specific orientation of the fibers and others 90° shifted to that. The carbon fibers are inside of thermoplastics, which most likely have very similar absorption characteristics as the Carbon fibers. We also now the number of these fibers is low. Performing a Flat Field correction, process mentioned in section subsection 3.2, we obtain our first look at the carbon sample measured, in the setup seen in Figure 10. A single projection at a given angle is seen in Figure 25. This image is taken with the X-ray tube at a voltage 25 kV and a current of 200 μA, a acquisition time of 1 second for the detector, and the sample at a distance of 7 mm from the source. This results in a magnification of around 44, using Equation 10. An iterative rotation angle of 0.2 degrees was taken, meaning for each slice the sample is rotated 0.2°. This carbon sample stands out, as it doesn't absorb much radiation. Bottom part of the image shows parts of glue, and the wooden platform, which is not perfectly flat. In other sections of the sample, that can be seen in the appendix in Figure 48, the wood structure can be more clearly seen. One would expect a low absorption in the carbon sample, given firstly its

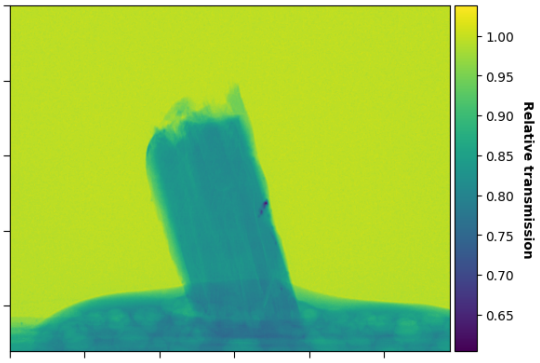

Figure 25: Flat field corrected transmission image of the carbon sample mounted in the rotational stage. As the image with object is divided by the background, radiation transmission from the detector is given in relative values, which can be seen in the colorbar in the right. Light blue colors mean a low absorption, darker blue colors mean a bigger absorption. Base of the image corresponds to the absorption of wooden base and glue that sticks the sample and base together. Rectangle object is the carbon sample.

low atomic number, and secondly the thin width. As is seen, almost all, around 0.8 of the radiation, is transmitted, however no microstructures or differences in transmission within the sample are shown. Also, in the inner middle part of the sample there is a small region with higher absorption, seen also from several other angles, possibly indicating another type of material that has glued to that part of the sample. Optically, no distinction can be made by looking at that point of the sample, indicating that the defect is within the material.

Another important point in the analysis are possible fluctuations, as x-ray tubes can experience fluctuations in their output, both in terms of voltage and intensity. In many x-ray systems, the voltage applied to the tube is not perfectly stable but fluctuates during the exposure. These voltage variations can directly affect the intensity and energy spectrum of the generated x-rays, rising above the preset value at the start of the exposure and then gradually decreasing to the set value or the other way around. Degradation in the tube can also affect the intensity terms. These fluctuations can be mainly affected by the refrigeration of the x-ray tube. The fluctuations in the very short timescales, which are usually called Ripples [16], are not considered here, as taking a reference image for each projection measured would increase too much the measurement time. We can however check for the long term fluctuations and perform a noise analysis to check the short term stability. In order to see the long term fluctuations, a flat field correction can be compared taking a background measurement before measuring the sample, and one after the full process is completed, which in the case of this thesis is about 2 hours.
There are no hard edges in Figure 26, which means that the source location seems to be stable. The differences in absolute transmission values between the images are in the range between 0.03 and -0.03, while the mean difference value is of 0.007, below a 1% change, indicating a very low level of change between the two images. To try to see fluctuations during the measurements, without actually taking a background

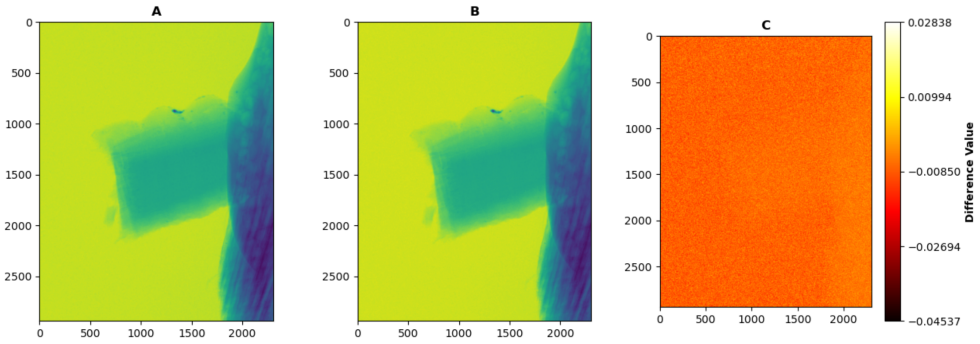

Figure 26: Image A shows a flat-field corrected image with background taken before measurements. Image B background is taken after the measurement of the sample is complete. Iamge C shows the difference in values between Image A and image B.

reference image after each projection, a free field noise analysis is done. The process done here is to take a small region of the image with no object. Then the mean value of the pixels inside that region is measured and compared with the rest of the images mean values of that same region. This allows us to see the change in the background values, which, ideally would not change. Taking a look at Figure 27, we see change is minimal, apart from the first 8 images, which are a bit of outliers. Again values stay within a small range. If we take the standard deviation of this curve we obtain a value of 0.001, meaning we can correctly measure changes in the transmission image up until 0.1%, the point where the noise doesn't allow more precision. This in turn allows us to confirm the very good overall stability of the x-ray tube in this micro-CT, so no corrections are needed to compensate for the fluctuations, as expected, in a x-ray setup without gratings.

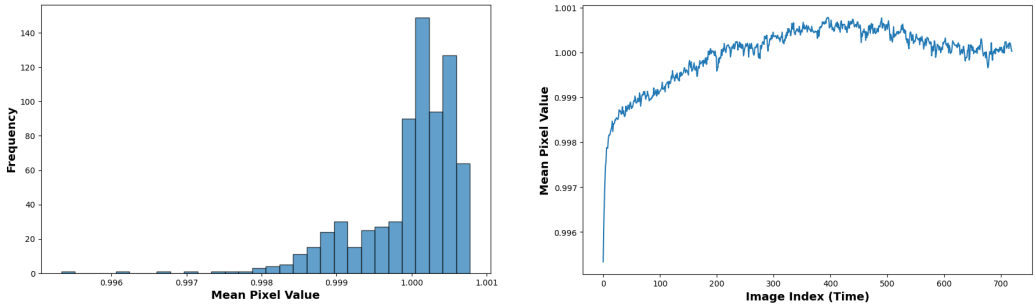

Figure 27: (Left) Histogram of Background Mean Values. This value is the mean value of all the pixels in a certain background zone without object, for all the flatfield corrected images taken. Values are shown in frequency, with a spike around 1.000. (Right) Fluctuation in Background Pixel Value Over Time. Curve plot of the background mean values for all the flatfield corrected images.

We can now take an even closer look at our carbon sample. Upgrading our setup, which could be seen in Figure 10, a thin rod is introduced, replacing the thicker metallic base rod, which can be seen in the final mount of the experimental setup, explained in section subsection 3.2, which allows for a stable rotation and the possibility to approach

the sample to distances of 1 mm. In this case, a new part of the carbon sample is approached 4 mm to the source.

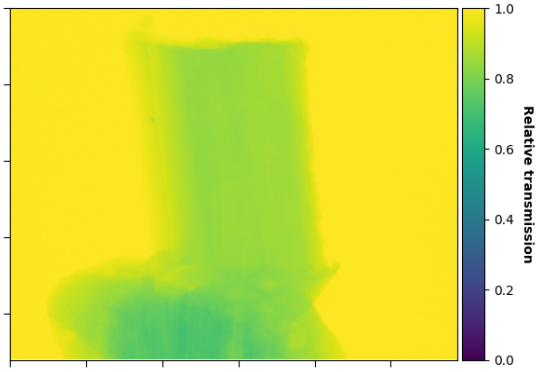

Figure 28: Flatfield transmission image of the carbon sample 4 mm away from the x-ray source, meaning a magnification of 77,5. Colorbar displays the relative absorption. In yellow, the background, yields almost unity values, as no object absorbs radiation. In green absorption objects are seen, darker colors mean bigger absorption. Carbon sample is seen as a rectangle. In the bottom of the image, a higher absorption object is seen, the rod from the rotation axis. The other light absorption form is the glue that sticks the rod and the sample together.

Again not a lot of absorption is seen. Absorption rate is very similar, altough a bit lower than before, due to the lower integration time. In any case one cannot still resolve any microstructure. In fact, no structure at all is seen on the sample, even with a 77,5 magnification factor. With this magnification, taking into account that:

$$S_{eff} = \frac{S}{M} \tag{27}$$

where S is the pixel size, S_{eff} the effective pixel size and M the magnification, and we have a pixel size of 0.049 mm, we find that our effective pixel size is approximately 65 nanometers. When at 7 mm the effective pixel size is of 115 nanometers approximately, so a bit more than a micron. We also need to take into account the focal spot size, which in this case, is of 3 micrometers. Cosidering everything our setup should be able to resolve and see microstructures of around 3 microns when sample is probed at 4 mm. In any case we don't see them. Even when taking a look at other angles, no perceivable structure is seen Figure 49. Having taken a look at two different parts of the carbon sample, figures show very similar absorption (apart from the strange point of absorption seen in Figure 25) but no microstructures whatsoever in the flatfield images, which could lead to think that this sample is an unstructured carbon piece or made from another material. We expected to see some layers of fibers, however, as the carbon fibers are inside of thermoplastics, which most likely have very similar absorption characteristics, the contrast is too small, so we do not see the fibers in the micro-CT transmission image. Taking into account our resolution limit and the noise of the detector we should be able to see the fibers inside this sample but we don't. The explanation for this can lie on the similarity of absorption between the thermoplastic layers that encapsulates the carbon fibers and the fact that we have very few carbon

fibers. In that case, with a sufficient amount of the thermoplastic material contrast wouldn't be enough to distinguish them from the carbon fibers. A 3D reconstruction will be later done to check if more information can be extracted from the projection images and a further analysis can be done on this sample. At this point, comparison with the titan sample becomes even more important, to check whether the setup works correctly and can actually resolve microstructures.

3.4 Titan Sample Analysis

In this part, the titan sample is probed and we have a look at the projection images obtained. For this a small piece of the sample seen in Figure 24 is cut away and glued onto the rotating rod. While we don't have a bibliography regarding the data of this sample, a previous lab work indicates that this sample has a fiber like structure, consisting on fibers of around 20 micrometers in diameter. Measurement process is the same as in subsection 3.3, however, as this sample absorbs a lot more of radiation, a first glance at the sample showed that varying the x-ray tube parameters allowed for a clearer image. The parameters used in the X-ray tube in this case for the titan sample are a voltage of 60 kV and a current of 400 μA. Titanium is a relatively high-Z element, so a higher absorption is precisely what one would expect. This increase in voltage and intensity has to be accounted in the measurement time of the detector. Acquisition time had to be reduced significantly, from 1 seconds to 0.3 s in order to compensate for the increase in count number. This is due to the detector saturating, reaching its maximum capacity, in turn giving an error. Source spot size also increases a bit when the voltage and current are increased, as discussed in subsection 3.1. In this case, we go from having a 3 micrometer source spot to a 5 micrometer source spot, which in turn means that the effective structure that this setup can resolve now is of around 5 micrometers, using Equation 1.

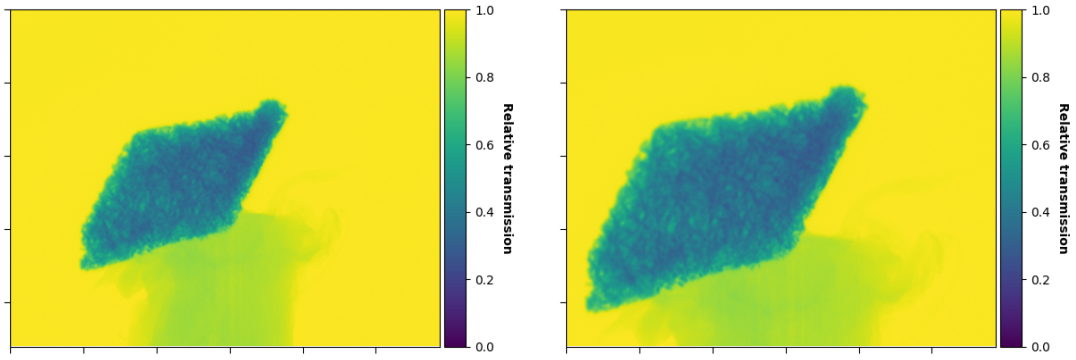

Figure 29: (Left) Flatfield image of the titan sample at a 6 mm distance from the source. Colorbar indicates the relative transmission. Sample is seen in dark blue. Green absorption objects shown in the bottom of the picture correspond to the rotation base rod, and the glue that sticks the sample and rod together, which absorb less radiation. (Right) Flatine image of the titan sample at 4 mm distance from the source.

In Figure 29 we can see two projection images, at 6 mm and 4 mm distance from the source. As one can see, the difference in size is clearly shown when we position the sample closer to the tube. The difference in absorption, as expected, is big between this

and the carbon sample. In this case, using again Equation 27, we have a magnification of around 51 when the sample is 6 mm away, and a magnification of 77,5 in the 4 mm case. No cracks or voids are seen, however we do see some type of structure showing already in the projection image, distinguished by the change in contrast. Fibers are seen, as some parts of the sample clearly absorb more radiation than others. This is a great indicator to show that the setup works, and that we can actually distinguish very small structures. In Figure 49 several angles of the sample are shown, where one can see the appreciable structure of the sample. These projections already indicate that a 3D reconstruction could yield a lot of information about the structures, and the following process will allow us to check whether these projection images are good enough to obtain a valuable CT-reconstruction.

4 3D Reconstruction

In this section, the 3D reconstruction of the investigated samples will be shown. For the reconstruction, the Dragonfly software was used [12]. Other softwares are available for the 3D reconstruction of CT projection images, but the one used in this thesis is the beta version of the CT reconstruction in Dragonfly. Dragonfly's CT Reconstruction module includes the bench-marked Feldkamp-David-Kress (FDK) algorithm for reconstructing 2D cone-beam projection data into 3D volumes, briefly looked at in section 2.2.1. In addition, geometry readers are provided for commercial CT scanners, however this was not used in this thesis. The parameters that the software takes are angle iteration, source to sample distance, source to detector distance, detector spacing, which means the pixel size of the detector, and detector and source offset. To note, the detector size in pixels is big (2940x2304 pixels), yielding datasets of more than 40 GB. This was something that this software couldn't handle. In order to be able to reconstruct the samples, cutting the images was needed to reduce the amount of data and in turn reduce the size of the array given to the software. Further explanations will be given for each of the images obtained.

4.1 Carbon Sample Reconstruction

The 3D reconstruction of the carbon sample was done with the images taken at 7 mm, meaning all the projections at all angles from the dataset of Figure 25, a single slice. As previously stated, images had to be cut in order for the size to be reduced. In this case, the full sample was kept in sight, as it didn't occupy the whole detector screen, however, the base was cut, as well as other parts of the image that only had background. This in turn is a potential error source, as the optical beam of the x-ray source is taken to be in the middle of the projection images. A parameter allows the correction in the x direction of the optical beam, however, the software does not clearly state what is done in the y direction. This can be a problem because we are working with cone beam geometry, and as stated in subsection 3.2, changes in the y direction might lead to a blur in the image. This is noted, as it can be a source of blurring that appears in our final reconstruction image. In all cases and for both samples, a ring removal filter was applied, as in all the reconstructions obtained a ring-type artifact was seen in the 3D display. These artifacts, which were discussed in Figure 2.2.1 show up here, and are corrected via filters, so that the final images are more clear.

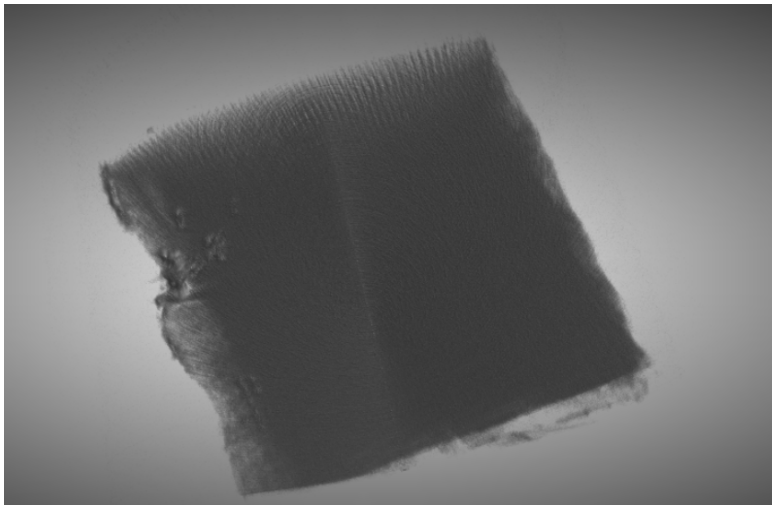

Figure 30: 3D reconstruction image of the carbon sample, from the micro-CT projections of the sample 7 mm away from the x-ray microfocus tube.

Unfortunately, it is hard to visualize a 3D object in a 2D thesis paper. This is much better visualized on a screen that can rotate and zoom in on the sample. However, we can see with the flatfield image the similar structure of the sample, which means reconstruction was successful. Once reconstruction is done, filters are applied to try and remove as many artifacts as possible, such a the ring removal filter, which tries to remove some rings that are usually formed in the CT images reconstruction [29]. Figure 30 shows the reconstruction of the carbon sample, which again, as expected seeing the projection images, yield an object with no clear structures. The edge of the sample can be clearly seen of the left part of the image, and some layered like structures can be barely seen at the top of the sample. This is again caused by artifacts, which were not removed by any filter, showing as well where there is no sample in the background, which is the clear confirmation that the structure that we see on the top is not caused by a real structure inside the sample, but really on the reconstruction process itself, which causes artifacts. We will see with the titan sample that we are able to reconstruct and measure fibers of 20 μm in size, and, in theory, with the magnification, we would be able to measure fibers of around 2 micrometers, depending on the detector noise and the real deviation from the rotation axis. So the reconstruction does not yield any additional information to the projection images obtained. What we can say is, because of the way this fibers are embedded in the thermo plastics, and these have similar absorption to the fibers, both are seen as the same in the micro-CT, which are the cause of not seeing anything. One would need to increase the contrast between these fibers and the plastics, for example with an even smaller focus spot, in order to distinguish them, to be able to characterize them properly.

4.2 Titan Sample Reconstruction

Titan Sample Reconstruction

Two 3D reconstructions were done for the Titan sample. Again this is due to the size of the dataset. For both data at 6 mm and 4 mm size was too big to handle in the reconstruction software. In the case of the 4 mm source to sample distance dataset,

in which the sample occupied the whole screen, cutting the edges was not enough, so a small piece of the sample was reconstructed, in turn not allowing a picture of the whole sample. Another dataset was used in order to see if a reconstruction of the whole sample was possible.

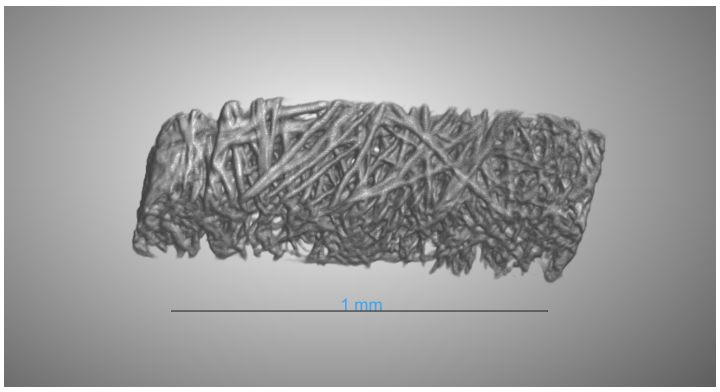

Figure 31: 3D reconstruction image of the titan sample, from the micro-CT cut projections of the sample 4 mm away from the x-ray microfocus tube. Line scale is provived at the bottom of the sample, where the distance equals 1 mm.

In the case of the 6 mm source to sample distance dataset, as the sample occupied less part of the screen, cutting the edges of the background was sufficient to reduce the size of the dataset for the software to handle. In Figure 31 and Figure 32 we see these two reconstructions of the sample. Both are plotted individually for better visualization. A ring removal filter was applied to both of them. In Figure 31 the reconstruction of a part of the 4 mm distanced sample is seen. Titan fibers are clearly seen in a darker gray, with a shadow like color at the edges. Reconstructing the whole 6mm distanced sample yields as well a very nice image, seen in Figure 32. For larger distances, magnification is decreased, which is the reason why the fibers look smaller. The whole picture is useful to get an idea of the overall look of the sample, as the fiber directions are more clearly seen in this full picture. As we can see, there are some preferential orientations of the fibers in the sample. There are some tools as well on the Dragonfly software that allow to obtain information about the fibers, as we will see in the following.

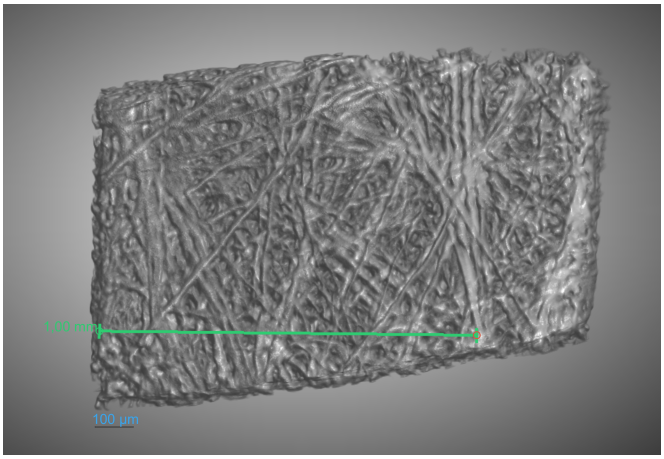

Figure 32: 3D reconstruction image of the full titan sample, from the micro-CT projections of the sample 6 mm away from the x-ray microfocus tube. Two scales are provided. One line in green, to contrast with Figure 31, equals 1 mm distance. In the bottom part of the sample, a line scale of distance 100 micrometers is shown.

In this thesis, the Dragonfly software is employed for the automated extraction and analysis of individual fibers from the titan sample. At first, the segmentation process uses the Open Fiber Segmentation algorithm [1], which provides an efficient approach for fiber identification and segmentation in 3D imaging data. The segmentation algorithm operates on a region of interest (ROI) that contains a mask (only values from a certain threshold are selected). After, it identifies each individual fiber and assigns a unique label to it, resulting in a multi-ROI output. If we take a look at a part of the reconstructed object obtained, we can see Figure 33, where colors (labels) are given to the detected fibers. Each label represents an instance of a distinct fiber within the dataset, enabling further analysis and characterization of the fiber properties. The process requires only minimal user input to define critical fiber parameters, including the minimum fiber length, the maximum stitching distance, which defines the maximum distance over which two disconnected fiber segments can be stitched together to form a single fiber, and a few other parameters which define how the fibers are searched. Once the fibers are segmented, the output dataset allows for a detailed analysis of the fibers' length and orientation distribution. By leveraging this automated fiber segmentation tool, the study would in theory efficiently process large datasets of fiber like structures, providing valuable metrics for material characterization without the need for extensive manual intervention. This method would significantly enhance the accuracy and scalability of fiber analysis. However, it wasn't able to work with a good enough accuracy for all the slices of the sample. As this is just a beta version, the software crashed and didn't correctly identify the fibers. This can be due to several factors. Firstly, the fibers touch each other, are interlaced, and a lot of them are joined together. This, because of the way the algorithm is built, makes it very difficult to separate the fibers from each other. Secondly, the images are a bit blurry. Here perhaps, the small misalignment and noise error from the detector plays a role, not allowing to obtain a better contrasted image, and, even though a lot of different input parameters were tested, perhaps not the optimal ones were inputted. This blur in the slices makes the segmentation process challenging.

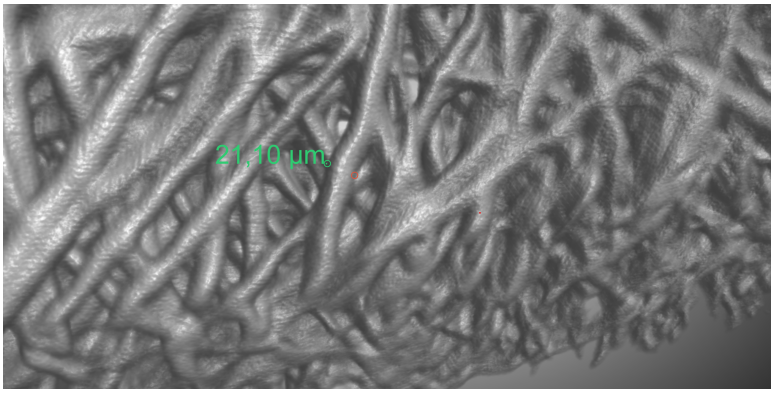

Figure 34: 3D reconstruction image of the cut titan sample, from the micro-CT projections of the sample 4 mm away from the x-ray microfocus tube. Two small green dots are marked, from one side of a fiber to the other, from which the software tool calculates a distance of 21.10 micrometers.

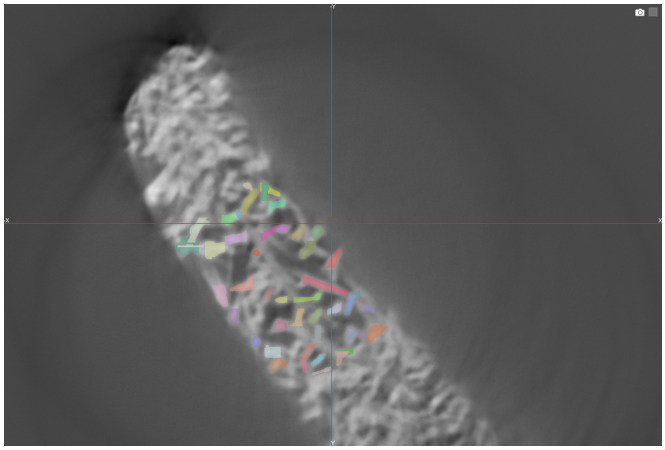

Figure 33: 2D slice of the reconstruction image of the cut titan sample, from the micro-CT projections of the sample 4 mm away from the x-ray microfocus tube. In colors, some fibers obtained through the fiber segmentation process are shown, others are wrongly identified fibers. Slice has some blur, which makes the segmentation process difficult.

Since automated software tools didn't work, manual intervention tools were needed in order to obtain information about the fibers. In a first step, a measuring tool was used to record the size (diameter) of several fiber. As seen in Figure 34, two marks are made manually, from which the software calculates the distance between the points. This visual tool is only an approximation, and can be done with a limited set of data, however, for this repeated process, a mean of 20.52 μm distance was obtained for 10 fibers, which correlates very well with the expected values of around 20 micrometers of fiber size, again taking into account 10 fibers is a very small set of data.

Then, fiber segmentation process is made manually. This is done by first applying a

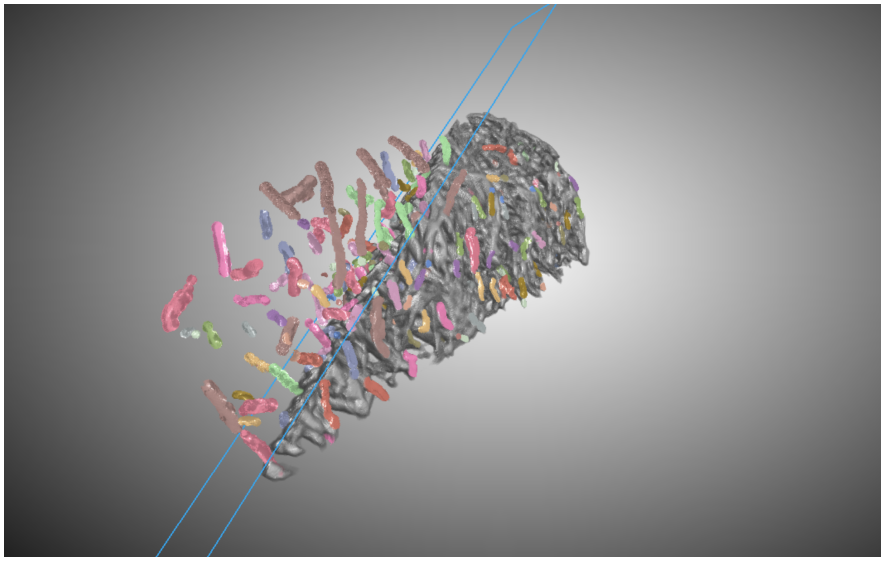

Figure 35: 3D reconstruction image of the cut titan sample, from the micro-CT projections of the sample 4 mm away from the x-ray microfocus tube. In colors, fibers obtained through the manual fiber segmentation process are shown. In blue, a plane is used to split the sample to be able to access the interior fibers.

limit threshold that allows us to select only the clearly defined fibers. Then, a 3D selection tool is used to manually 'paint' the fibers in the 3D image. For this another tool is used in order to access the interior part of the sample, and not only select the outside fibers, which is the plane split. This essentially creates a plane and allows to make a part of the sample invisible. This process can be pictured in Figure 35, where we see colored fibers, as well as a plane tool that allows to split the sample in order to access the interior fibers. This method has two problems to take into account. Not all the fibers are painted, which means that we could be inducing a preferred direction of the fibers just by painting in a certain direction and leaving other directions unselected. This is a problem with most humans, as they are not good enough at making random things. Secondly, selection tool is not always precise. We can not paint fibers that overlap or touch each other. This is because the segmentation process is done after the selection, meaning once we paint, the program connects all the components in the region of interest and assigns a label to each of the obtained fibers. If we select two distinct fibers that touch each other this software will identify it as one single fiber, again misleading when we compute measurements. Some individual pixels are sometimes selected by mistake, inducing error in the posterior analysis of the fibers. This is why selected fibers with less than 60 pixels are deleted. And also, the selection tool might sometimes only paint the outside of the fiber, the fiber partially or directly not paint some part of the fiber that was selected by the user. This process is not as optimal, however, in the end gives some good estimates and fibers selected are actually fibers, unlike in the automatic process, where a lot of the labels were put on random spots.

Figure 35 shows the manual fiber segmentation process, and how the fibers are labeled. Lots of fibers are however left unlabeled, so this has to be taken into consideration when analyzing the results obtained. We can now compute some measurements regarding the

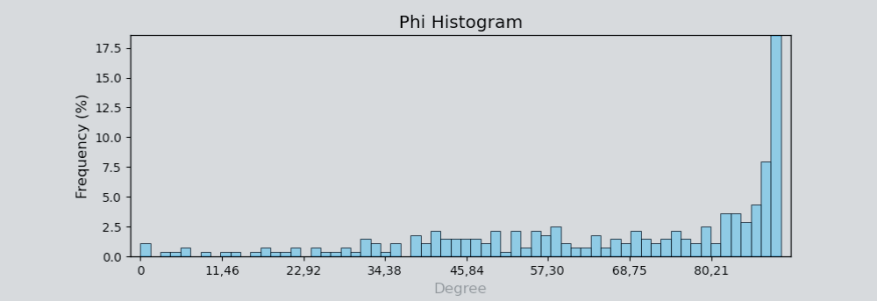

Figure 36: Histogram of the frequency as a function of the ϕ angle of the fibers' orientations.

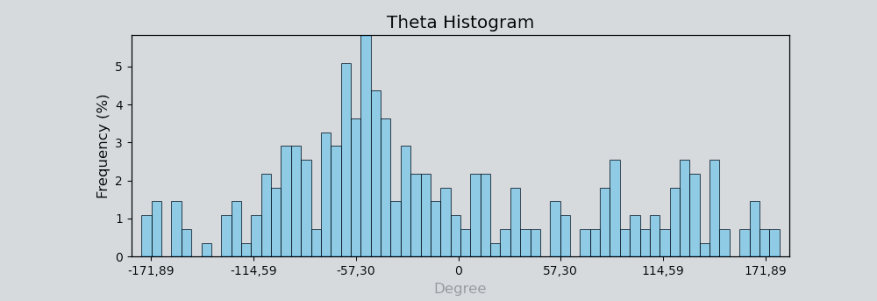

Figure 37: Histogram of the frequency as a function of the θ degree of the fibers' orientations

manually selected fibers. This is again done automatically by the Dragonfly software. Computed in the world coordinate system, Phi and Theta describe the orientation of the longest axis of the sample. This is visually shown in Figure 38. The phi (ϕ) angle, Figure 36, which can range from 0 to 90 degrees, is the angle between the Z axis and the longest axis of the object. The histogram shows a significant peak around 80°-90°. This indicates that most fibers are oriented nearly perpendicular to the x-axis in the xy-plane, suggesting a preferred alignment of fibers in a specific direction. The concentration at this range might reflect the sample's production or preparation process, such as a fibrous orientation due to external forces like stretching or processing, so essentially, how this sample was manufactured. A small spread is seen in all other directions, showing there is a small amount of fibers aligned in every direction. On the other hand, the theta (θ) angle, Figure 37, which can range from -180 to 180 degrees, is the angle between the X axis and the projection of the longest axis of the object on the X-Y plane. A peak of orientated fibers can be seen at an angle around -57,30°. These preferred orientations, which can already be seen in some way in the 3D reconstruction figure of the sample, are confirmed in these histograms. These orientations suggest that we should obtain some sort of signal in the dark-field image, as these changes in orientation fibers should yield a phase change. These results are to be taken carefully, as we have said, the segmentation process can lead to a lot of errors, so while the results are what we would expect, this can only be taken as an estimate.

We could also compute the particle radius mean, which would in turn give the diameter of the fibers, information that we can contrast well. However, due to the segmentation

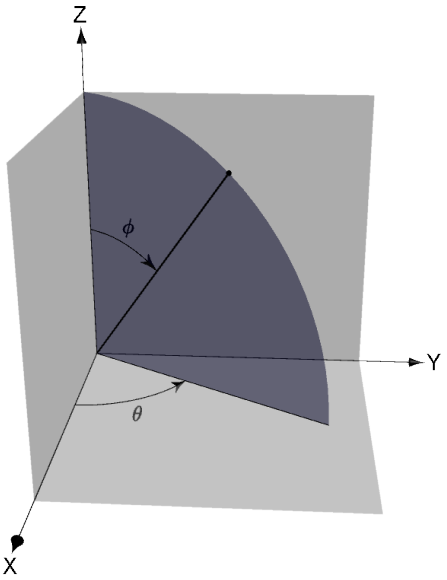

Figure 38: Sketch of the representation of Phi (ϕ) and Theta (θ), which describe the orientation of the longest axis of the sample. ϕ is the angle between the Z axis and the longest axis of the sample while θ is the angle between the X axis and the projection of the longest axis of the sample on the X-Y plane.

process used to select the fibers this structure size measurement cannot be done in detail. To many errors are present on this computation, so no more information was extracted from the sample.

5 Directional Dependent Darkfield Imaging

In this chapter, we will look at both samples previously examined, switching to the grating-based dark-field imaging setup. An initial analysis of the data obtained in this setup will be performed for both samples. A comparative analysis will also be done, with previous information obtained in the CT imaging. An overview of the theoretical part was given in subsection 2.3, however an overview of the actual setup will be given in the following.

5.1 Setup of Phase-Contrast Scanner

The measurement setup used in this thesis is a grating-based Talbot-Lau X-ray interferometer in the form of a vertical scanner setup, with the source being the Titan-neo tube [34]. Parameters, shown in Table 3, are set to obtain the highest visibility (30 to more than 50 %) for wide spectra at acceleration voltages between 40 and 70 kV [5]. The X-ray source is an ISOVOLT Titan neo X-ray generator and an X-ray tube with a tungsten anode [4]. There is a 2 mm thick aluminum protective filter and an additional 0.2 mm thick copper protective filter, which is located at the exit window of the X-ray tube and yields a more suitable x-ray spectrum for this imaging system.
Figure 39 shows a photograph and the schematic layout of the scanner setup. The absorption grating G0 is an absorbing grid, which provides the necessary spatial coherence of X-ray radiation through which the Lau effect, referred to in subsection 2.3 is produced. The phase lattice G1 is a $\pi/2$-shifting grating. Approximately at a fractional Talbot distance from G1, the absorption grating G2, which serves as an analyzer grating and is assembled together. The distance from which the grating G2 is put from G1 is checked with simulations, as the Talbot distance is energy dependent, and this setup is a polychromatic system, meaning that the intensity patterns of all energies overlay. The phase grating G1 and the analyzer grating G2 are composed of several 10 $\times$ 50 mm individual gratings. The phase stepping curves depend on the alignment of the individual lattices relative to each other and differ therefore partially from one another. The individual lattice parameters of the structure are shown in Table 1. The grating height corresponds to the thickness of the mesh along the optical axis and the duty cycle gives the ratio between the width the lattice bars and the lattice period.

Grating	**G0**	**G1**	**G2**
Material	Au	Au	Au
Period [µm]	13.31	5.71	10.00
Grating Height [µm]	200.0	6.3	200.0
Duty Cycle	0.66	0.30	0.50
Source Distance [mm]	150	750	1190

Table 3: Grating Parameters of the Setup.

The detector is a CMOS detector (Shad-o Scan 4501) which works by integrating energy, meaning that it measures the total energy deposited per pixel [10]. A reference image without an object is captured using the phase stepping method for image acquisition,

explained in subsection 2.3. To do this, the source grid is moved by 2 grating periods into approximately 80 equidistant points. When the object is recorded, the movement is replaced by the movement of the object. Scanning reconstruction process is fully explained in [5].

Figure 39: (Left) A photograph of the scanner setup is shown. The orange X-ray tube is located in the lower part of the image, above which is the G0. The scanning table is located between the G0 and the G1 and is moved horizontally during the scan, above which the rotation controller is put. The G2 is positioned at approximately a fractional Talbot distance from G1. Above that, there is a detector 1385 mm away from the source. (Right) Schematic representation of the scanner setup. The scanning direction is the x-direction. The grating, detector, and object table are in the x-y plane. The lattice bars are oriented along the y-axis. The optical axis runs in the z-direction. Image taken from [32].

This reference analysis of the setup's visibility is shown in Figure 40. The section in the middle is taken as the zone to place our samples, as it shows the highest visibility values. Values of maximum visibility go up to 70%, but the mean visibility used is around 55%, which is very good for this type of setup.

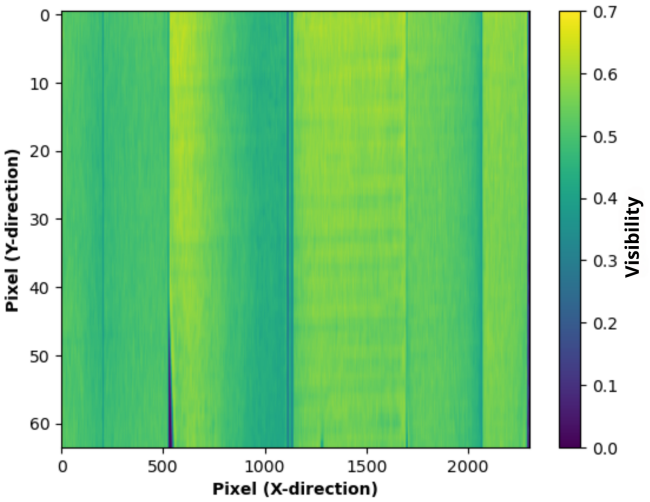

Figure 40: The visibility map of a reference recording at 50 kV accelerating voltage can be seen. Shown in the image is only the zone used for the measurements, as the values obtained outside this zone were affected by the rotating stage.

5.2 Image Acquisition and Artifact Correction

Firstly, it is of importance to note that in this setup we are measuring both carbon and titan samples. However, as the characteristics of the micro-CT setup only allowed a very small sized sampled to be measured, only parts of less than 1 mm extracted where shown. Here however the full samples, seen in Figure 24, are probed, as the analysis of a smaller object becomes much harder in this detector (magnification on the other detector had a very big value), and we also want to check if we can see the different orientations present in the carbon sample. The entire samples are taken, as seen in Figure 24, one of the main advantages of dark-field imaging, as we can examine a significantly large field of view within a short span of time. The samples were placed in a rotation axis that allowed the 360° rotation in the x-y plane. This plane where the sample is put onto the scanner table is the same as the one in the reconstruction process, subsection 4.2, which allows us to directly contrast the information obtained. Images were taken at iterations of 10°, producing a total of 36 images for each sample. The parameters for the x-ray tube were 50 kV in voltage, 12 uA in current, values optimized for this grating setup, where the current is nearly at its maximal value for the voltage applied [5]. Integration time of the detector was of 50 milliseconds. Taking a first look at the obtained images we see a lot of noise can be produced in the images, especially in the dark-field, as these images are very sensitive to changes and perturbations. The carbon sample, as expected, does not produce a lot of absorption.

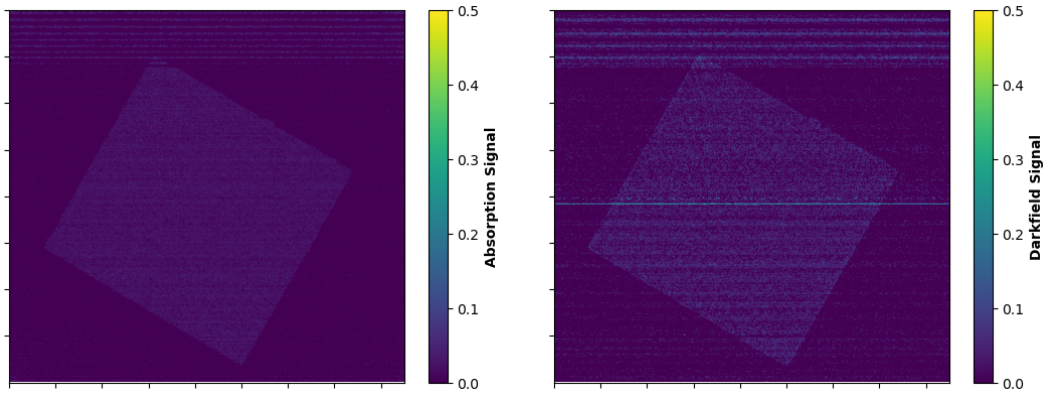

Figure 41: (Left) Absorption image of the carbon sample in the grating setup. (Right) Dark-field image of the carbon sample. Lighter tones of blue mean a higher absorption. The square that is tilted represents the sample. Blue horizontal lines appear, which are scanning artifacts.

In Figure 42, the dark-field image is noisier in the upper part than in the bottom. There is a blue horizontal line in the middle of the image, and at the top these lines repeat themselves often. If we take this into numbers, the mean standard deviation from the middle up is a bit higher than from the middle down. This can be caused by some thermal influences, but more likely the gratings don't work as well as they are supposed to. Either there are some defects in the grating or the gain correction does not correctly work here. In any case, dark-field imaging is very sensitive to small scattering, so noise is more easily introduced than in the absorption image.

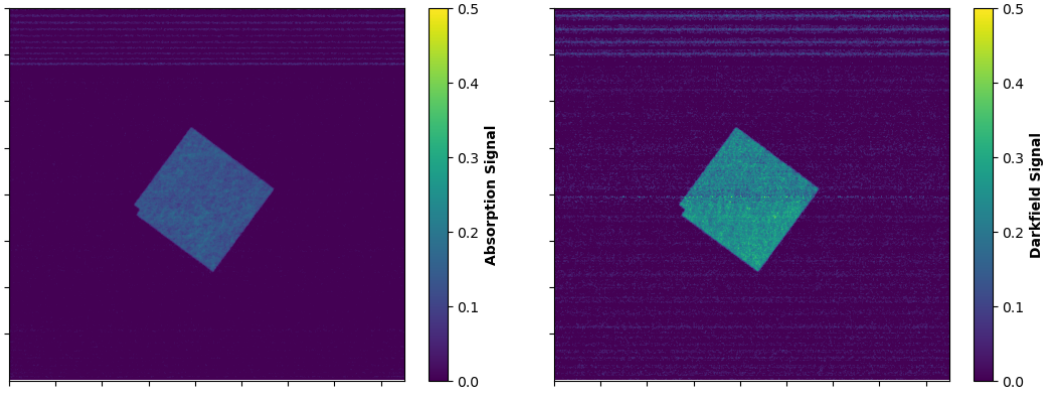

Figure 42: (Left) Absorption image of the titan sample in the grating setup. (Right) Darkfield image of the titan sample. Lighter tones of blue mean a higher absorption. The square that is tilted represents the sample.

In dark-field images, unwanted background gradients or instrument artifacts can reduce subtle phase variations from the sample. We can introduce a filter to try and correct these artifacts. The filter used here, is designed to remove background variations in dark-field images. The goal is to obtain a "flattened" image where the background is closer to zero. In the following figures, the artifact corrected images from both samples are shown.

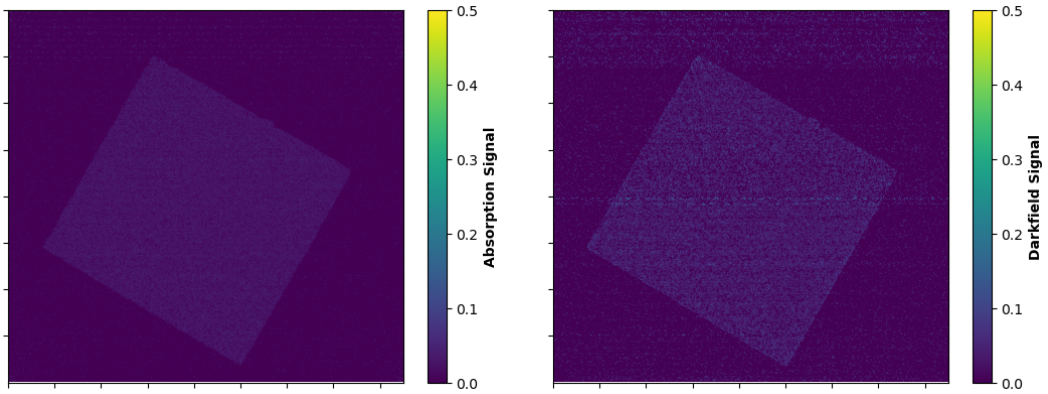

Figure 43: (Left) Filtered absorption image of the carbon sample in the grating setup. (Right) Filtered darkfield image of the carbon sample.

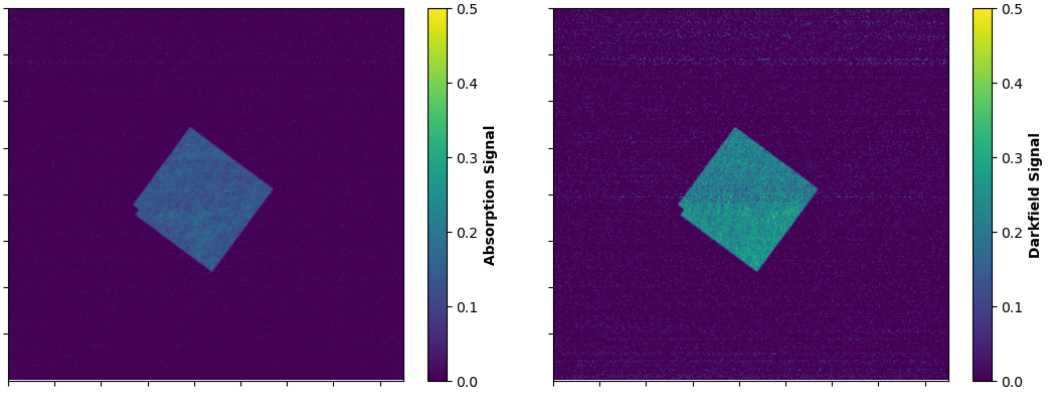

Figure 44: (Left) Artifact corrected absorption image of the titan sample in the grating setup. (Right) Artifact corrected dark-field image of the titan sample. Lighter tones of blue mean a higher absorption.

These images are clearer from artifacts, even though they are not completely removed. As visible in Figure 44 (Right), from the middle up there are still more artifacts than from middle part down. This is an effect, probably caused by defects in the gratings, that will have an impact in later analysis.

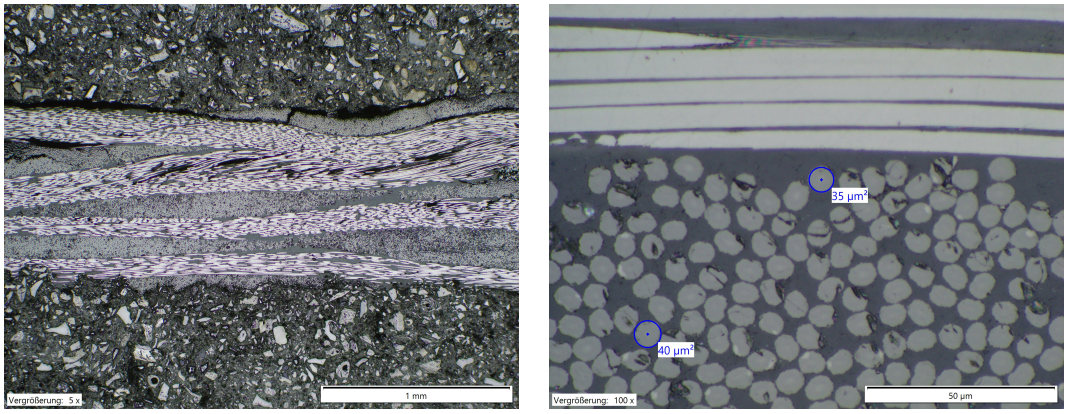

Figure 45: (Left) 50x magnified image of the carbon's sample structure. Seen are small fibers embedded in thermoplastic layers.. (Right) 1000x magnified image, where the fibers at a 90° angle can be seen. Blue circles are put in a couple of fibers, showing their size. These images are not a result from a measurement of this thesis, but an external measurement from which information was extracted, and are shown here to illustrate the real structure of the carbon sample.

The initial observations align well with the micro-CT data, as the carbon sample consistently exhibits low absorption and scattering. This is primarily due to the overlapping and perpendicular arrangement of the carbon fibers, which leads to destructive interference and consequently a diminished carbon signal, as illustrated in Figure 43. Also, the number of fiber appears to be small to generate a big signal. The images in Figure 45 were extracted from another setup that was not used here or part of this thesis, and are given as an illustration of the carbon structure and why it might present its behavior both in the micro-CT and grating-based setups. Although one might anticipate a stronger signal given the presence of fibers, of around 40 micrometers, that could induce scattering, the observed outcome, a weak signal, is both expected and consistent with the sample's structure. Unfortunately, even with this setup only the information known can be contrasted, but no new information can be gained from the grating-based scanner.

Meanwhile, the titan sample shows more absorption, again expected, as in the flatfield image, taking into account the high Z value of the titanium, and a significant value in the dark-field image. This was to be expected, from subsection 4.2, as the preferred orientations from the fibers predicted a signal in the dark-field image. We can now perform a further analysis on the dark-field images of both samples to try to contrast this first information outlook, and also to see whether more information can be extracted.

5.3 Darkfield Image Analysis

One of the main interests in this thesis is to correlate the data obtained in the micro-CT, regarding the microstructure characteristics, with the data obtained in dark-field imaging. For that we will analyze the dark-field signal images of both samples. From the already filtered ones, analysis is performed by identifying a small part of the sample, called region of interest (ROI), seen in Figure 46 in red, taking the mean value of all the pixel values from that region and repeating the process following that same ROI when the sample is rotated. This process can be seen in the appendix, in Figure 51.

This same method was used for both the carbon and titan samples. That way we can check for directionally dependent absorption in the samples, which would indicate the presence of a directionality preference in the fibers orientations. This is because, as briefly overviewed in subsection 2.3, changes in the dark-field indicate different direction of the microstructure present in the sample. In this setup, highest values would be yielded if the fibers were orientated in the direction of the gratings, and zero signal would be seen if all the fibers were orientated at a 90° angle from the grating.

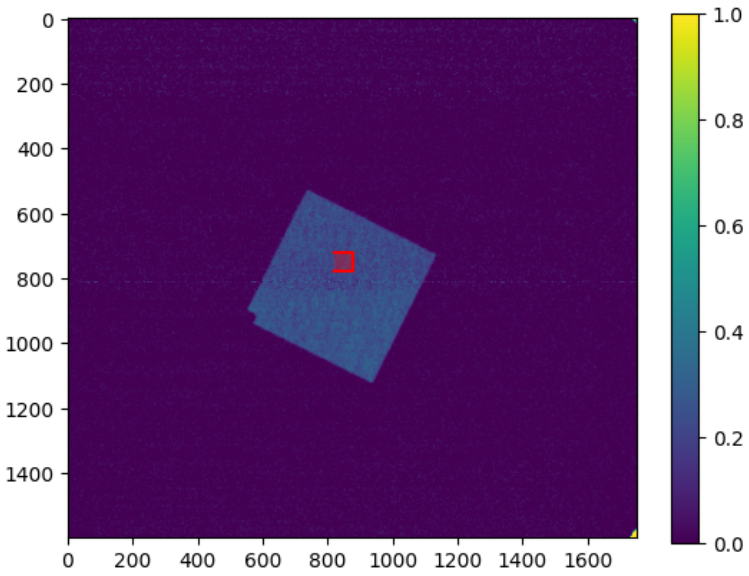

Figure 46: Filtered darkfield image of the titan sample. Colorbar shows the relative signal. Region of interest is displayed as a red square. From this region the values averaged over all of the pixels of this zone are taken over all the 36 obtained images to check for direction dependant absorption.

This method encounters a problem when stepping in and out of the artifact in the middle, and, in general, with the artifacts in the image. This is why the position of the ROI has to be considered carefully, to try to avoid as much the artifact region. Center of rotation of the sample is also a key parameter to determine in order to be able to correctly assign the rotation of the sample to the rotation of the ROI and measure the same zone of the sample for all images. This is key, as different parts of the sample can exhibit different behaviors, depending on the fibers properties.

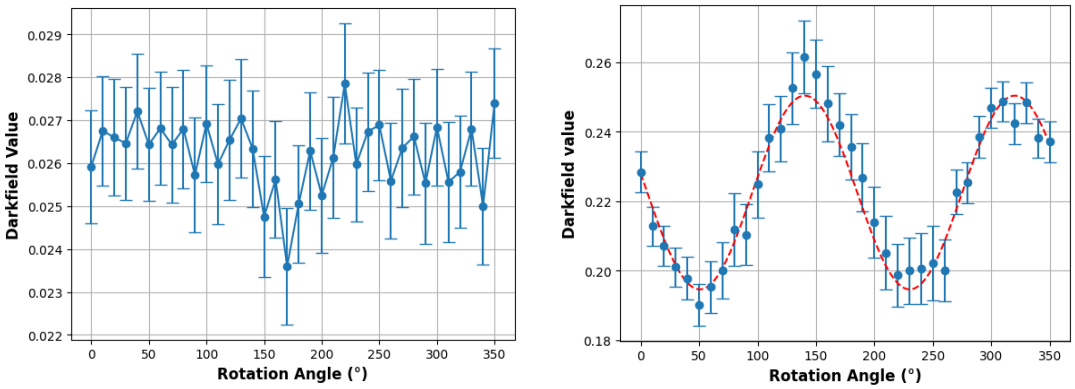

Figure 47: (Left) Mean values of the pixels in the region of interest for the dark-field image of the carbon sample. (Right) Mean values of the pixels in the region of interest for the dark-field image of the titan sample. In red dotted lines, a sin function fitted to the data is shown.

Shown in Figure 47, the mean dark-field values for the ROI of the samples are shown over all the angles probed. Carbon sample shows an almost linear response, indicating little to none direction dependent absorption. This was expected, as a the overlay of the different layers present in the carbon sample, which have different orientations, has in principle no directional dependence. When we go to the (right) display, we can see a sine like behavior in the titan sample. A sine function is fitted into the data to visually display the behavior of the dark-field values when the sample rotates. This shows that the fibers are not isotropically distributed but that there is a mean direction of the fibers, which makes sense, considering the preferred orientation angle from the titan fibers seen in the 3D reconstruction. As discussed in Figure 2.3.4, a perpendicular orientation from the fibers with respect to the grating would yield no dark-field signal. Here, a minimum at around 50 and 230 degrees is shown. The minimum at 50° is coincident with the fiber orientation peak of -57 degrees obtained in subsection 4.2, and when rotated as well with the following minimum. The estimations calculated in the reconstruction seem to correlate well with the data obtained in this setup. Taking a look at the absorption of the samples, very similar absorption ranges are seen in the micro-CT setup, although different x-ray tube settings are used to measure each sample in each setup, which is why different absorption spectra are seen for the same sample, but in a very similar range. Carbon sample absorbs much less radiation than the titan sample in both setups. Looking as well as the analysis of the dark-field signal, the low signal of the carbon indicates these overlapped fiber directions, which don't produce a lot of scatter, whereas the preferred orientation of the titan fibers in turn produce a much stronger signal. This complementary analysis of the samples is an indicator that the micro-CT images and data obtained can serve as reference images for the grating-based setup. One can correctly obtain data from the micro-CT that one can correlate with the grating-based setup. Computed calculations however, especially in the fiber segmentation part, were much of an estimation, so this previous statement again has to consider all the possible error sources.

6 Outlook and Conclusion

To summarize the findings, this thesis has managed to set up a working micro-CT, that has micrometer resolution, aligning it with to the detector plane with an innovative approach. It has estimated the characteristics of a titanium sample, imaging its microstructure, where fibers of around 20 micrometers in diameter could be seen. It also correctly characterized the direction and preferred orientations of these fibers, as was checked with the dark-field images of the sample. The information from the already established Talbot-Lau interferometer setup correlated well with the data obtained from the micro-CT, and further reinforced our micro-CT findings as well as the possibility to complement these two setups in future measurements. Micro-CT images can serve as reference images for the grating-based setup and can yield information on what to expect before measuring the sample in the Talbot-Lau interferometer. However, it was not able to correctly characterize and image the microstructures from the carbon sample. As discussed in subsection 4.1, the complex layout of the sample, where the supposed small number of fibers was embedded in a thermoplastic material that had similar absorption, did not allow to show this microstructures in any image. From this, insight can also be gained, as it has shown not every structure can be imaged in this setup. A more comprehensive analysis is left in order to study which types of these complex structures cannot be imaged in the micro-CT setup, and which errors could be further corrected (alignment and detector noise) in order to improve the resolution and sensitivity.

This thesis has demonstrated the capability of imaging microstructures using micro-computed tomography (micro-CT), establishing it as a powerful, almost non-destructive method, as you need to have either a small sample, or cut your way to a sample that can fit in the detector, in order to reveal the internal structure of materials at the microscale. Through careful acquisition, reconstruction, and analysis of 3D datasets, we have shown that micro-CT enables a rich, spatially resolved characterization of samples, particularly when investigating morphological features such as fibers. However, further improvements into the software reconstruction and fiber parameter measurements is needed in order to obtain more accurate data. Fibers could be clearly seen in the titan sample, however the interlacing of them posed a problem for their segmentation and posterior analysis.

Beyond conventional absorption-based contrast, the work has also explored the complementary strengths of grating-based X-ray phase-contrast imaging, with a particular emphasis on the dark-field signal. Unlike absorption imaging, which is primarily sensitive to differences in material density and composition, the darkfield modality is uniquely sensitive to unresolved microstructures, such as fiber orientations, grain boundaries, or sub-resolution scattering centers that would otherwise remain invisible. In this regard, dark-field images add a new dimension of contrast, capturing textures and fine structural information that complements the morphological insights gained from micro-CT reconstructions, although the main data obtained from the samples in this thesis came from the micro-CT setup and its reconstruction. The integration of both imaging approaches reveals a compelling synergy: micro-CT provides a volumetric baseline, offering an intuitive, high-resolution map of the sample's interior, which can really serve as a contextual guide or validation reference for the interpretation of phase

and dark-field images. Conversely, the dark-field signal offers sensitivity to features below the resolution limit of the CT scanner, enhancing the interpretation of subtle features observed in 3D reconstructions and guiding more targeted structural hypotheses. We have showed that the combination of both can yield a complementary and correct analysis of sample's microstructures.

In summary, this thesis validates the concept that 3D microstructural imaging using micro-CT can serve as reference to guide the grating based dark-field imaging, that offers complementary information. The microstructure imaging, when approached through a combination of micro-CT and grating-based dark-field imaging, provides a rich and multiscale perspective. It allows us to not only see what is there, but to understand how internal features are distributed, how they interact, and what role they may play in the sample's function or behavior. This integrated imaging approach holds immense potential for advanced material characterization and could serve as a foundation for future developments in hybrid imaging systems where structure, composition, and microtexture are all resolved simultaneously.

To finalize, it has also shown not every sample carefully prepared for a bachelor thesis can yield a positive result, as not a lot of valuable information could be extracted from the carbon sample. Future challenges regarding this thesis would be the investigation of new ways to accurately image complex sample structures, with different layers with similar absorption. Also, the optimization of data storage, the polish and optimization of the reconstruction algorithms, in order to obtain a more detailed and accurate object 3D reconstruction, as well as the improvement in fiber segmentation process, not only in optimization, but also in the calculation of fiber parameters. A lot of these software processes are still in the beta version, so future optimization work is certainly something we can look up for.

A Appendix A

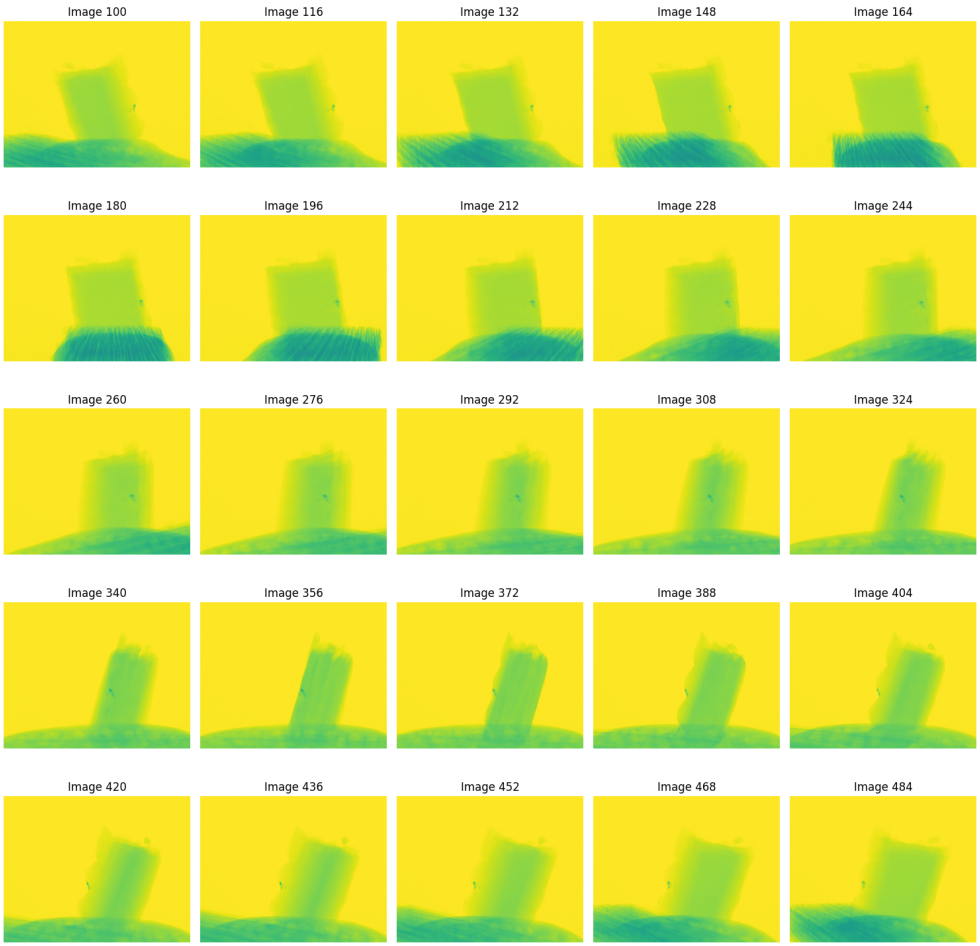

Figure 48: Absorption images for several angles of the carbon sample. Flat-field correction is applied.

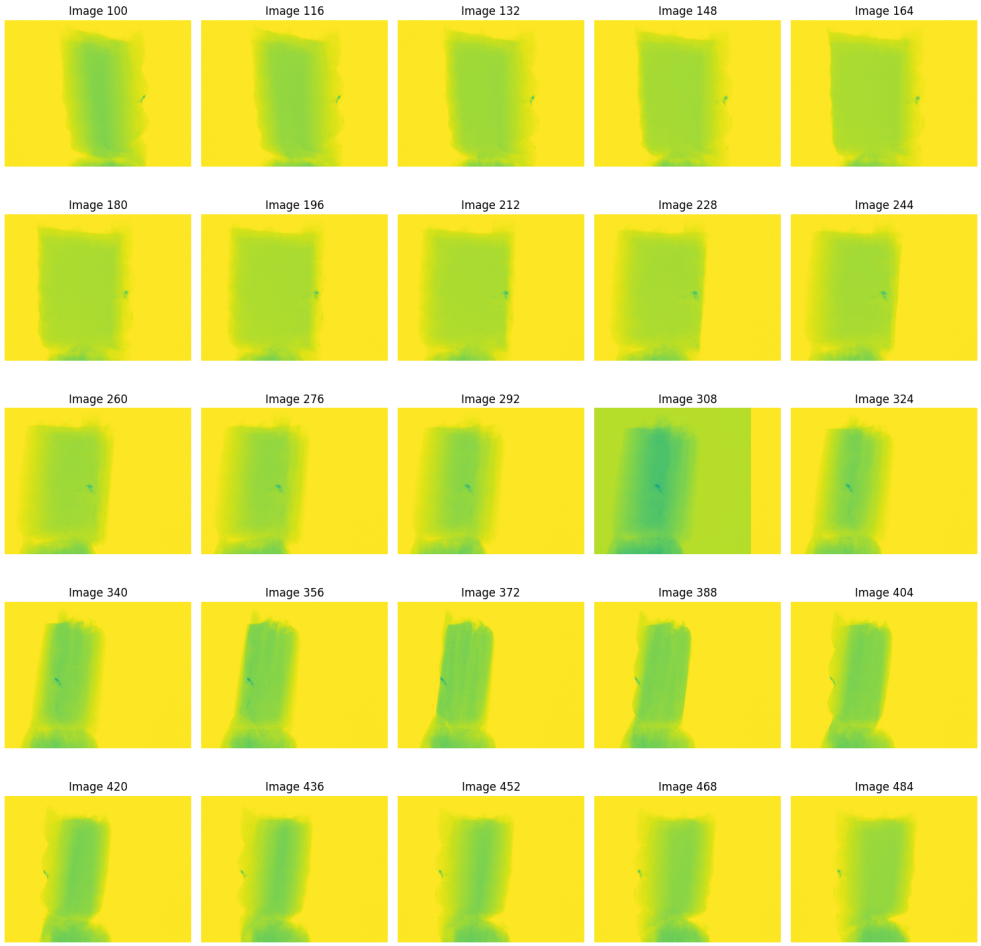

Figure 49: Absorption images for several angles of the carbon sample, 4 mm away from the source. Flat-field correction is applied. Image on column 4, row 3, "Image 308" has a strange background color, different from the rest, probably due to a background value error.

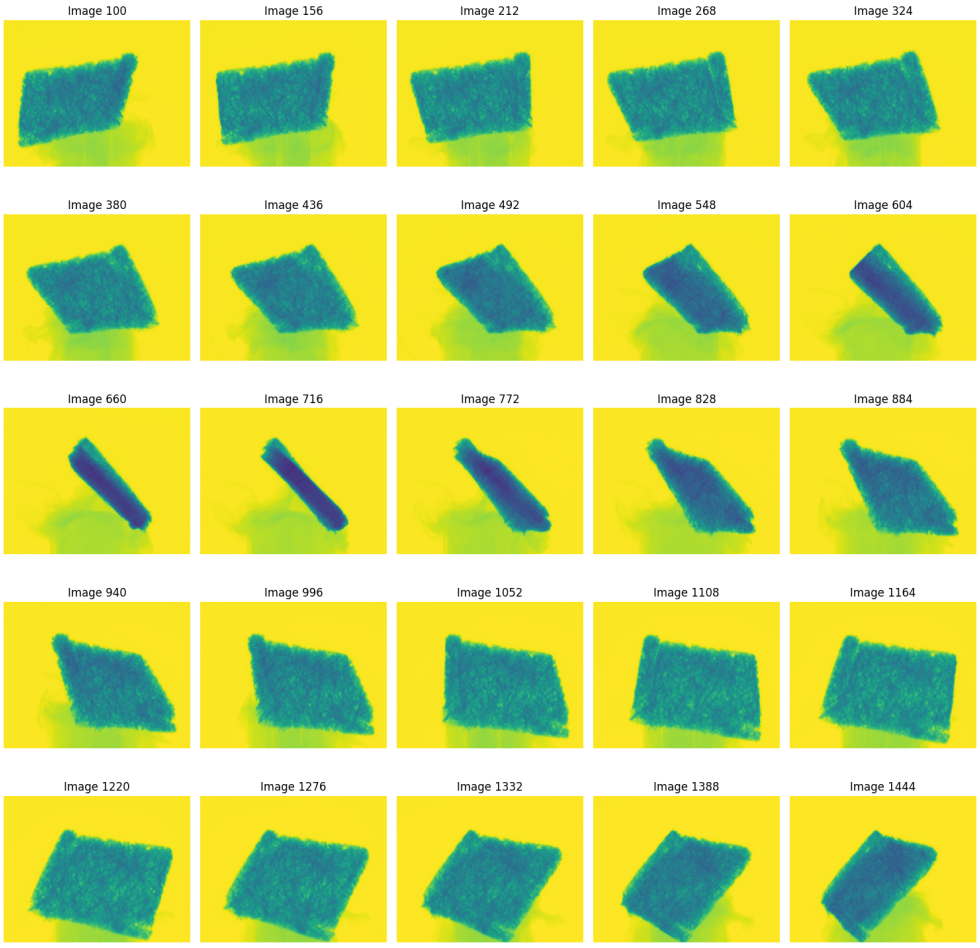

Figure 50: Absorption images for several angles of titan sample, 4 mm away from the source. Flat-field correction is applied.

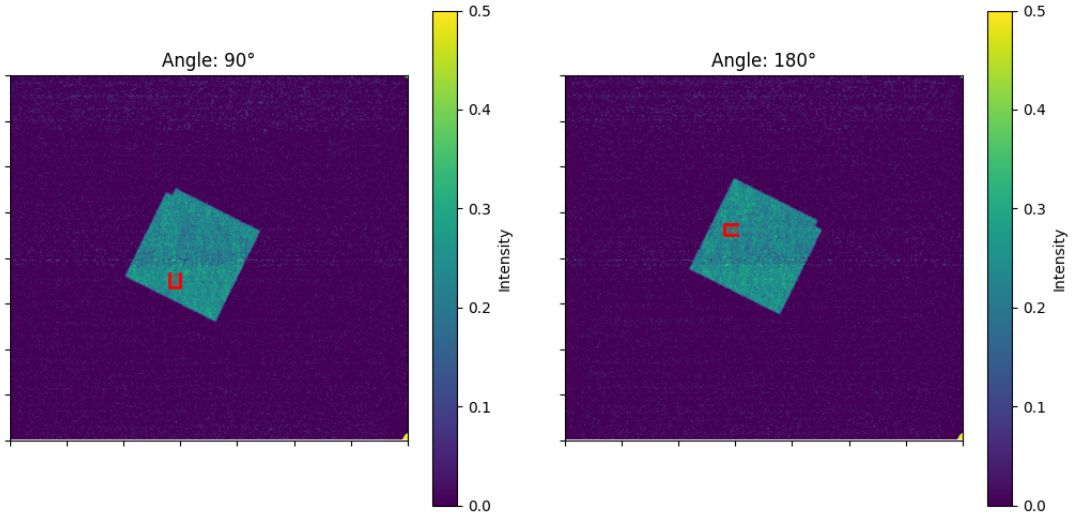

Figure 51: Analysis process of the darkfield images of the titan sample in the grating-based phase-contrast imaging setup. Sample is rotated in iterations of 10° and a region of interest marked in red takes all the pixel values from the zone and averages them. In this case the process for the 90 (left) and 180 (right) degree rotation is displayed. Colorbar displays the absorption values in percentage.

Bibliography

[1] Facundo Sosa-Rey et al. *Open Fiber Segmentation*. https://github.com/lm2-poly/OpenFiberSeg. [Online; accessed 22-June-2025]. 2025.

[2] "Attenuation Coefficient". In: (2025). DOI: doi:10.1351/goldbook.A00516. URL: https://doi.org/10.1351/goldbook.A00516.

[3] S D Auweter, J Herzen, M Willner, S Grandl, et al. "X-ray phase-contrast imaging of the breast—advances towards clinical implementation". In: *British Journal of Radiology* 87.1034 (Jan. 2014), p. 20130606. ISSN: 0007-1285. DOI: 10.1259/bjr.20130606. eprint: https://academic.oup.com/bjr/article-pdf/87/1034/20130606/54340387/bjr.20130606.pdf. URL: https://doi.org/10.1259/bjr.20130606.

[4] Bakerhughes. "Waygate Technologies". In: (). DOI: https://dam.bakerhughes.com/m/587c40904a269525/original/bhcs34152_de_ISOVOLT_Titan_neo_Generator_Fact_Sheet_R1.pdf. URL: https://dam.bakerhughes.com/m/587c40904a269525/original/bhcs34152_de_ISOVOLT_Titan_neo_Generator_Fact_Sheet_R1.pdf.

[5] Nora Balewski. *Qualitätsmessungen eines Talbot-Lau-Scanners und Strukturanalyse mittels Dunkelfeldbildgebung*. Bachelor Thesis, ECAP. 2025.

[6] Z. Messali Boudjelal Abdelwahhab and Abderrahim Elmoataz. ""A Novel Kernel-Based RegularizationTechnique for PET Image Reconstruction"". In: *Technologies 5* (2017). DOI: https://doi.org/10.3390/technologies5020037.

[7] Bruker. *Rotation step in micro-CT. How many projections do I need? Method note MCT-122*. https://www.foa.unesp.br/Home/pesquisa/escritoriodeapoioapesquisa/mn122_rotationstep.pdf. [Online; accessed 10-July-2025]. 2019.

[8] Thorsten Buzug. *Computed Tomography: From Photon Statistics to Modern Cone-Beam CT*. Springer Nature, 2008. ISBN: 978-3-540-39408-2.

[9] E. Dall'Ara, M. Boudiffa, C. Taylor, D. Schug, et al. "Longitudinal imaging of the ageing mouse". In: *Mechanisms of Ageing and Development* 160 (2016), pp. 93–116. ISSN: 0047-6374. DOI: https://doi.org/10.1016/j.mad.2016.08.001. URL: https://www.sciencedirect.com/science/article/pii/S0047637416301324.

[10] Teledyne Dalsa. *Shad-o-Scan 3001/4501 Datasheet*. https://www.daheng-imaging.com/uploadfile/2022/0223/20220223105350959.pdf. [Online; accessed 21-July-2025]. 2021.

[11] Wolfgang Demtroder. *Atoms, Molecules and Photons: An Introduction to Atomic-, Molecular- and Quantum Physics*. Springer Nature, 2019. ISBN: 978-3-662-55523-1.

[12] Dragonfly. *Dragonfly Webpage*. https://dragonfly.comet.tech/. [Online; accessed 21-DJuly-2025]. 2025.

[13] L. A. Feldkamp, L. C. Davis, and J. W. Kress. “Practical cone-beam algorithm”. In: *J. Opt. Soc. Am. A* 1.6 (1984), pp. 612–619. DOI: 10.1364/JOSAA.1.000612. URL: https://opg.optica.org/josaa/abstract.cfm?URI=josaa-1-6-612.

[14] Luca Fritsch. “Characterization of a Grating-Based Dark-Field CT System”. In: *Msc.Thesis FAU* (2025).

[15] Artur Omar Gavin Poludniowski and Robert Bujila. *NIST - XCOM: Photon Cross Sections Database*. https://www.nist.gov/pml/xcom-photon-cross-sections-database. [Online; accessed 20-July-2025]. 2021.

[16] André C. Carneiro et al. Geraldo P. Araujo Arno H. Oliveira. “FLUCTUATIONS ON THE X-RAY INTENSITY BEAM USING A PORTABLE X-RAY PROBE BASED ON 6LiI(Eu) CRYSTAL.” In: *2011 International Nuclear Atlantic Conference - INAC 2011* (2011). DOI: doi:10.1351/goldbook.A00516.

[17] FineTec FineFocus Technologies GmbH. *FOMM160*. https://www.finetec-technologies.eu/index.html. [Online; accessed 20-July-2025]. 2024.

[18] Noam Weiss Lana Volokh Haim Azhari John A. Kennedy. *From Signals to Image*. Springer Cham, 2020. ISBN: 978-3-030-35325-4.

[19] Gabor T. Herman. *Fundamentals of Computerized Tomography*. Springer Nature, 2009.

[20] S. D. Dover. J. C. Elliott. ““X-ray microtomography””. In: *Journal of Mycroscopy* (). DOI: https://doi.org/10.1111/j.1365-2818.1982.tb00376.x.

[21] Veronika Ludwig. “Development of image acquisition and alignment methods for X-ray dark-field and phase-contrast imaging”. PhD thesis. FAU-ECAP. Erlangen Center for Astroparticle Physics, 2020.

[22] Schultz K et al. Mudgal P Vangala T. “Characteristic radiation”. In: *radioapedia.org* (). DOI: https://doi.org/10.53347/rID-25429. URL: https://radiopaedia.org/articles/25429.

[23] Iowa State University Center for Nondestructive Evaluation (CNDE). *Geometric Unsharpness*. https://www.nde-ed.org/Physics/X-Ray/GeometricUnsharp.xhtml. [Online; accessed 10-July-2025]. 2021.

[24] David Paganin. *Coherent X-Ray Optics*. Oxford University Press, Jan. 2006. ISBN: 9780198567288. DOI: 10.1093/acprof:oso/9780198567288.001.0001. URL: https://doi.org/10.1093/acprof:oso/9780198567288.001.0001.

[25] Gavin Poludniowski, Artur Omar, Robert Bujila, and Pedro Andreo. “Technical Note: SpekPy v2.0—a software toolkit for modeling x-ray tube spectra”. In: *Medical Physics* 48.7 (2021), pp. 3630–3637. DOI: https://doi.org/10.1002/mp.14945. URL: https://aapm.onlinelibrary.wiley.com/doi/abs/10.1002/mp.14945.

[26] Johann Radon. ““Uber die Bestimmung von Funktionen durch ihre ¨ Integralwerte l¨angs gewisser Mannigfaltigkeiten””. In: *Berichte der Sächsischen Akademie der Wissenschaften zu Leipzig* (1917).

[27] Constantin Rauch. “Setup characterisation measurements for grating-based X-ray phase-contrast imaging”. MA thesis. FAU-Erlangen Center for Astroparticle Physics, 2022.

[28] André Ritter, Peter Bartl, Florian Bayer, Karl C. Gödel, et al. “Simulation framework for coherent and incoherent X-ray imaging and its application in Talbot-Lau dark-field imaging”. In: *Opt. Express* 22.19 (2014), pp. 23276–23289. DOI: 10.1364/OE.22.023276. URL: https://opg.optica.org/oe/abstract.cfm?URI=oe-22-19-23276.

[29] Stuart R Rock. *MicroComputed Tomography: Methodology and applications*. CRC Press, 2020. ISBN: 978-1-498-77497-0.

[30] Robert S. Pozos Rüdiger Kramme Klaus-Peter Hoffmann. *Springer Handbook of Medical Technology*. Springer Berlin, Heidelberg, 2011. ISBN: 978-3-540-74657-7.

[31] R. Schofield, L. King, U. Tayal, I. Castellano, et al. “Image reconstruction: Part 1 – understanding filtered back projection, noise and image acquisition”. In: *Journal of Cardiovascular Computed Tomography* 14.3 (2020), pp. 219–225. ISSN: 1934-5925. DOI: https://doi.org/10.1016/j.jcct.2019.04.008. URL: https://www.sciencedirect.com/science/article/pii/S1934592519300607.

[32] Ludwig-V. Kaeppler S. et al. Seifert M. “Talbot-Lau x-ray phase-contrast setup for fast scanning of large samples.” In: *radioapedia.org* (2018). DOI: https://doi.org/10.1038/s41598-018-38030-3.

[33] Teledyne Vision Solutions. *Shad-o-Box HS*. https://www.teledynevisionsolutions.com/de-de/products/shad-o-box-hs/?vertical=tvs-dalsa-x-ray&segment=tvs. [Online; accessed 20-July-2025]. 2024.

[34] WayGate Technologies. *Seifert ISOVOLT-Röntgenröhren für industrielle Röntgen- und CT-Generatoren*. https://www.bakerhughes.com/de/waygate-technologies/industrial-radiography-and-ct/xray-tubes-and-generators/isovolt-xray-tubes. [Online; accessed 20-July-2025]. 2024.

Acknowledgements

I would like to thank everyone in my path through the physics bachelor, and especially:

- Professor Stefan Funk, for supervising and allowing me to be in his medical physics group and do this thesis.
- Professor Vojislav Krstic, for his help throughout my journey here at FAU.
- Professor Beatriz Porras, and the Universidad de Cantabria, for caring and adapting to my needs.
- All the colleagues of the MedPhys group, specially to Markus Schneider, Constantin Rauch and Stephan Schreiner, for their constant help throughout this bachelor thesis, their ideas and their guidance.
- To all my friends in Spain, and here in Germany, that have motivated me to continue working hard during my bachelor.
- To my family, for their constant support and for allowing me the opportunity to live this experience in Germany, for which I am grateful for.

Declaration of Originality

I, Juan Prior Herrero, student registration number: 23585041, hereby confirm that I completed the submitted work independently and without the unauthorized assistance of third parties and without the use of undisclosed and, in particular, unauthorized aids. This work has not been previously submitted in its current form or in a similar form to any other examination authorities and has not been accepted as part of an examination by any other examination authority.

Where the wording has been taken from other people's work or ideas, this has been properly acknowledged and referenced. This also applies to drawings, sketches, diagrams and sources from the Internet.

In particular, I am aware that the use of artificial intelligence is forbidden unless its use an aid has been expressly permitted by the examiner. This applies in particular to chatbots (especially ChatGPT) and such programs in general that can complete the tasks of the examination or parts thereof on my behalf.

Any infringements of the above rules constitute fraud or attempted fraud and shall lead to the examination being graded "fail" ("nicht bestanden").

Place, Date	Signature